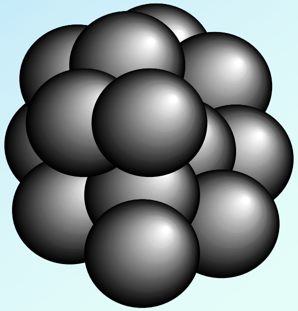

物理化学特論IV
クラスターの科学
第二部

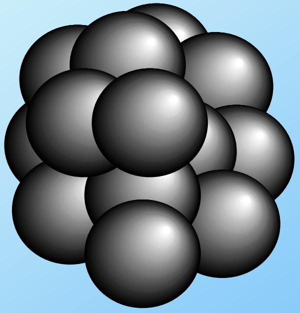

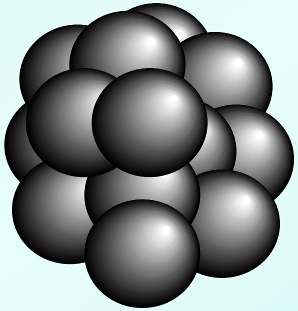

講義内容（予定）

クラスターとは？

1. 金属クラスターの電子構造1；水銀クラスター, 金属ー非金属相転移
2. 金属クラスターの電子構造2；アルカリ金属クラスター，電子殻模型と魔法数, 原子核とクラスターとの類似性と異質性
3. 分子クラスターの反応とダイナミクス；$I_2^-(CO_2)_n$，光解離と再結合, 微視的な溶媒効果
4. 遷移金属クラスターと気体分子との反応
5. クラスターの衝突反応
6. タンパク質のフォールディング;Levinthalのパラドックス
7. 気相タンパク質イオンの立体構造の変化;イオン移動度の測定
8. 生体分子の質量分析における新技術
9. 孤立状態において生体分子を研究する; Angiotensin Iイオンと気体分子の温度変化によるプロトン移動反応

講義内容（予定）

クラスターとは？

1. 金属クラスターの電子構造1；水銀クラスター, 金属ー非金属相転移
2. 金属クラスターの電子構造2；アルカリ金属クラスター，電子殻模型と魔法数, 原子核とクラスターとの類似性と異質性
3. 分子クラスターの反応とダイナミクス；$I_2^-(CO_2)_n$，光解離と再結合, 微視的な溶媒効果
4. **遷移金属クラスターと気体分子との反応**
5. **クラスターの衝突反応**
6. タンパク質のフォールディング;Levinthalのパラドックス
7. 気相タンパク質イオンの立体構造の変化;イオン移動度の測定
8. 生体分子の質量分析における新技術
9. 孤立状態において生体分子を研究する; Angiotensin Iイオンと気体分子の温度変化によるプロトン移動反応

♣ 遷移金属クラスターと気体分子との反応

Supersonic metal cluster beams of refractory metals: Spectral investigations of ultracold Mo2

J. B. Hopkins, P. R. R. Langridge-Smith, M. D. Morse, and R. E. Smalley

The Journal of Chemical Physics **78**, 1627 (1983)

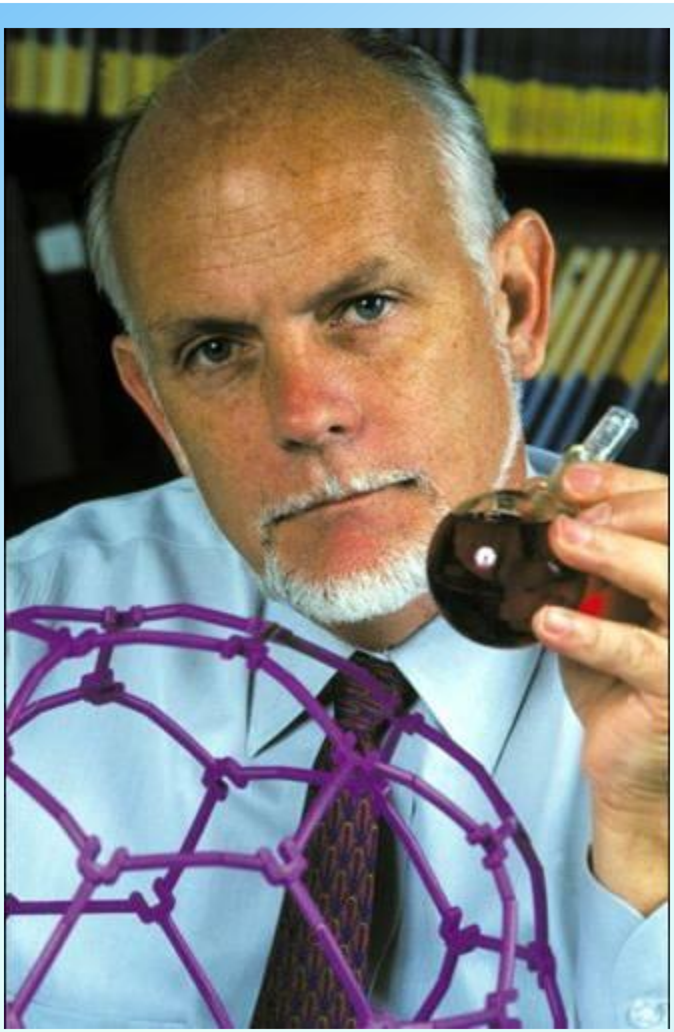

R. E. Smalley

1943-2005年

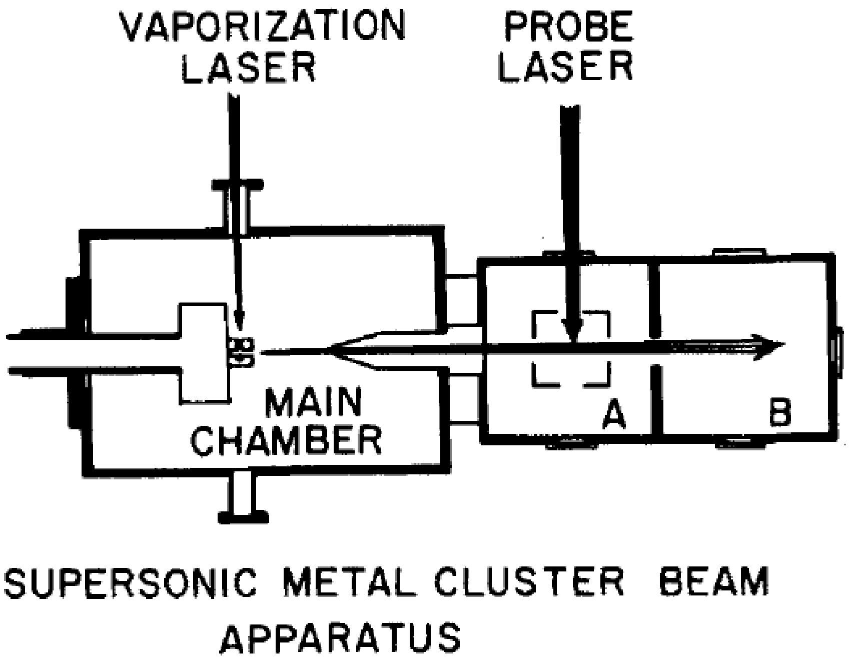

FIG. 1. Overview of the experimental apparatus. The main chamber skimmer is a 5 mm diameter conical skimmer mounted 21 cm off of the bulkhead and 20 cm from the nozzle. The distance between the nozzle and mass spectrometer is 57 cm. Typical average base pressures with the pulsed molecular beam on and off are: 8×10^{-5} ON/3×10^{-6} OFF Torr, 1×10^{-6} ON/1×10^{-8} OFF Torr, 4×10^{-8} ON/1×10^{-8} OFF Torr for the main A and B chambers, respectively. These values apply to a helium backing pressure of 8 atm and 10 Hz operation of the pulsed valve.

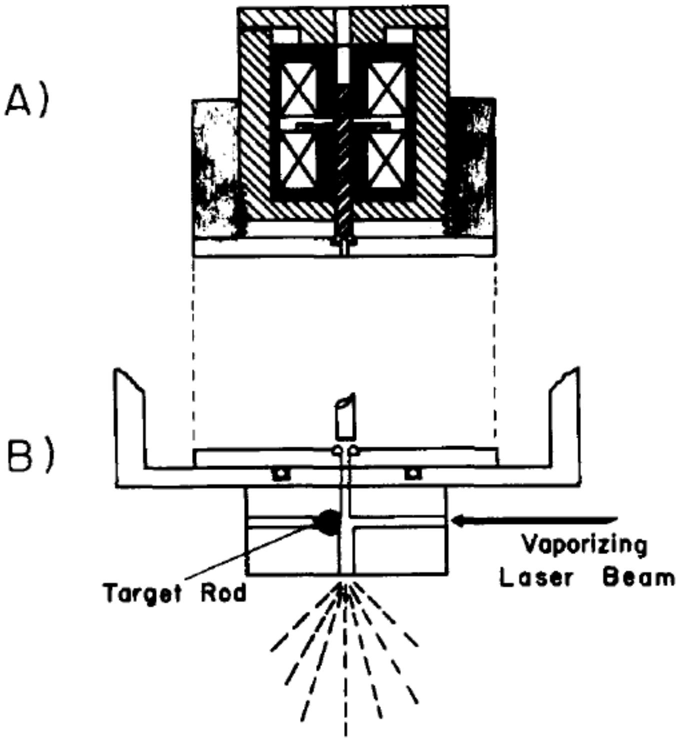

FIG. 4. (A) Schematic of the pulsed double-solenoid valve mechansim. The magnetic actuator, positioned between the pole faces of the two solenoid cores, is 1.58 mm thick, 25.4 mm in diameter, and has a travel of 1 mm when the valve is fully open. A utility spring (not shown) is located at the top of the magnetic actuator to maintain the seal of the actuator against the *O*-ring (Parker 2-002) when the solenoid current is off. (B) Metal cluster expansion faceplate. The channel leading from the actuator to the metal target rod is 22 mm long and 1.3 mm in diameter. The extension channel length from the target rod to the point of free expansion is varied between 3 and 30 mm and is 2.36 mm in diameter as shown. The laser axis channel bore is 25.4 mm long and 1 mm in diameter.

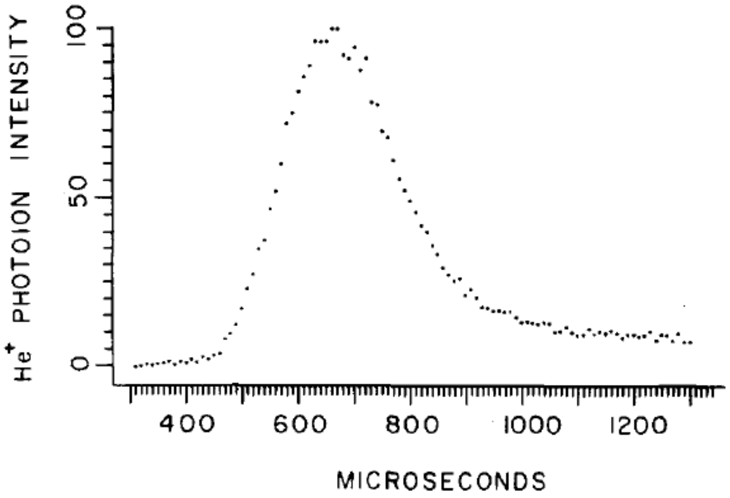

FIG. 5. Time of arrival of the skimmed helium beam in the photoionization region of the mass spectrometer. Photoions are produced by an ArF laser with a fluence of $\sim$1 mJ/cm^2. The time of arrival is measured by monitoring the intensity of He$^+$ photoions (*y* axis) as a function of the delay between the nozzle and ArF laser trigger pulses (*x* axis). The distance between the nozzle and mass spectrometer was 57 cm. The nozzle-to-skimmer distance was 20 cm. Expansion conditions were: helium backing pressure = 8 atm, orifice diameter = 1 mm, extension channel length = 3.0 cm.

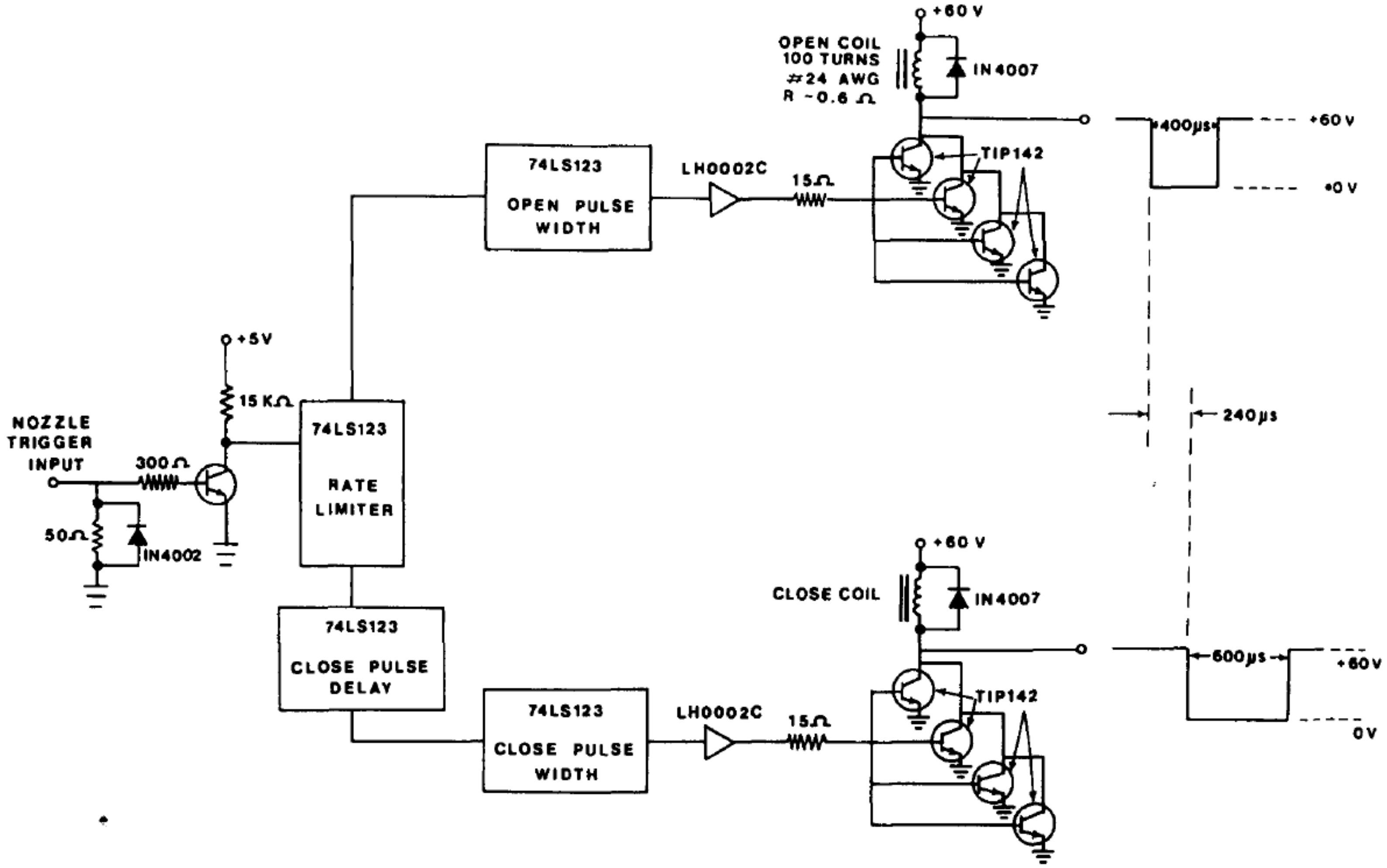

FIG. 6. Electronic schematic of the pulsed nozzle driving circuit. The input trigger pulse is + 2*V* to + 5*V* TTL. The repetition rate is limited to 12 Hz to restrict the average current through the TIP 142 current transistors.

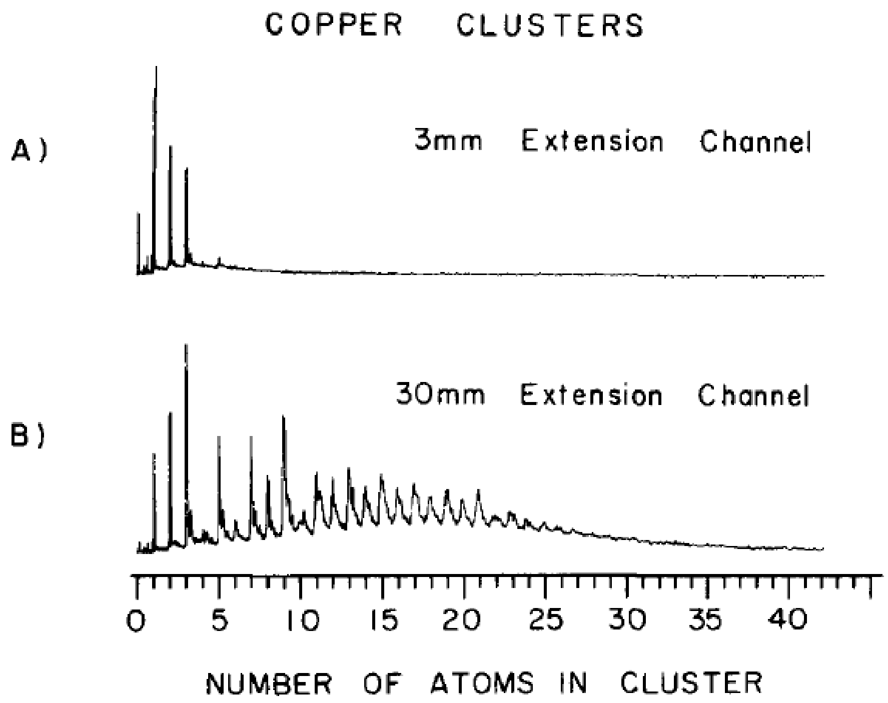

FIG. 2. Copper cluster size distributions resulting from the formation of clusters in two different length extension channels Both (A) and (B) time-of-flight mass spectra were recorded under identical mass focusing conditions of the spectrometer. Photoions were produced with an ArF (193 nm) laser at ~1 mJ cm^2. The nozzle backing pressure was 10 atm helium. Note that the additional features which occur in the mass spectra are due to copper oxides Cu_xO_y.

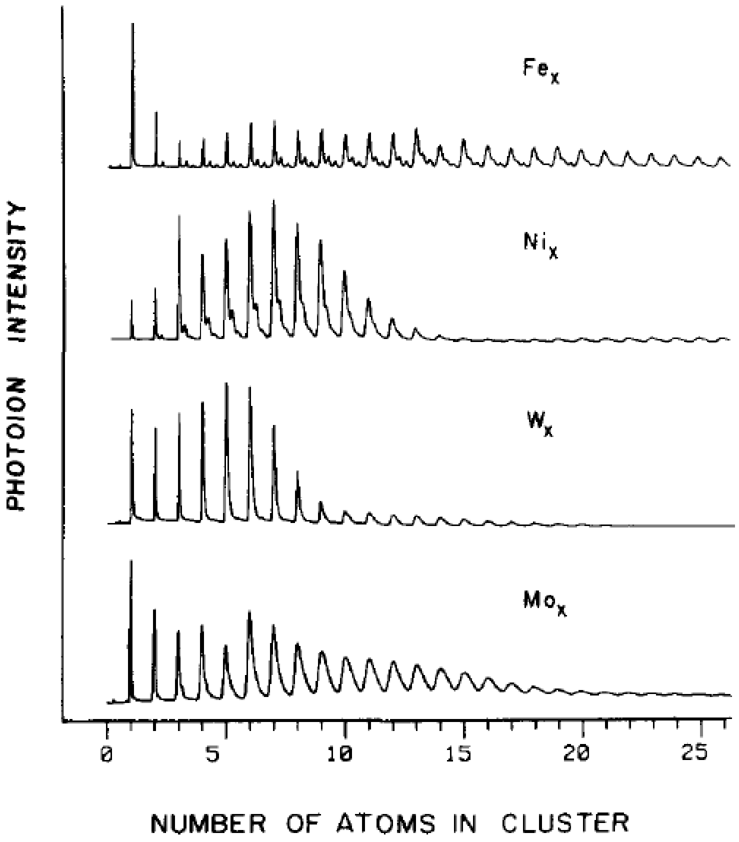

FIG. 3. Time-of-flight mass spectra illustrating cluster size distributions obtained from metal beams of iron, nickel, tungsten, and molybdenum. Photoions were produced by an ArF (193 nm) excimer laser with a fluence of ~ 2 mJ/cm^2. The nozzle backing pressure was 8 atm of helium which expanded through a 1 mm orifice. After laser vaporization clusters were formed in an extension channel 2.5 cm long and 3 mm in diameter. The mass spectra of Fe_x and Ni_x contain additional features due to metal oxides M_xO_y. The features in the molybdenum mass spectrum are broadened by the various isotopic modifications due to the seven naturally occurring molybdenum isotopes.

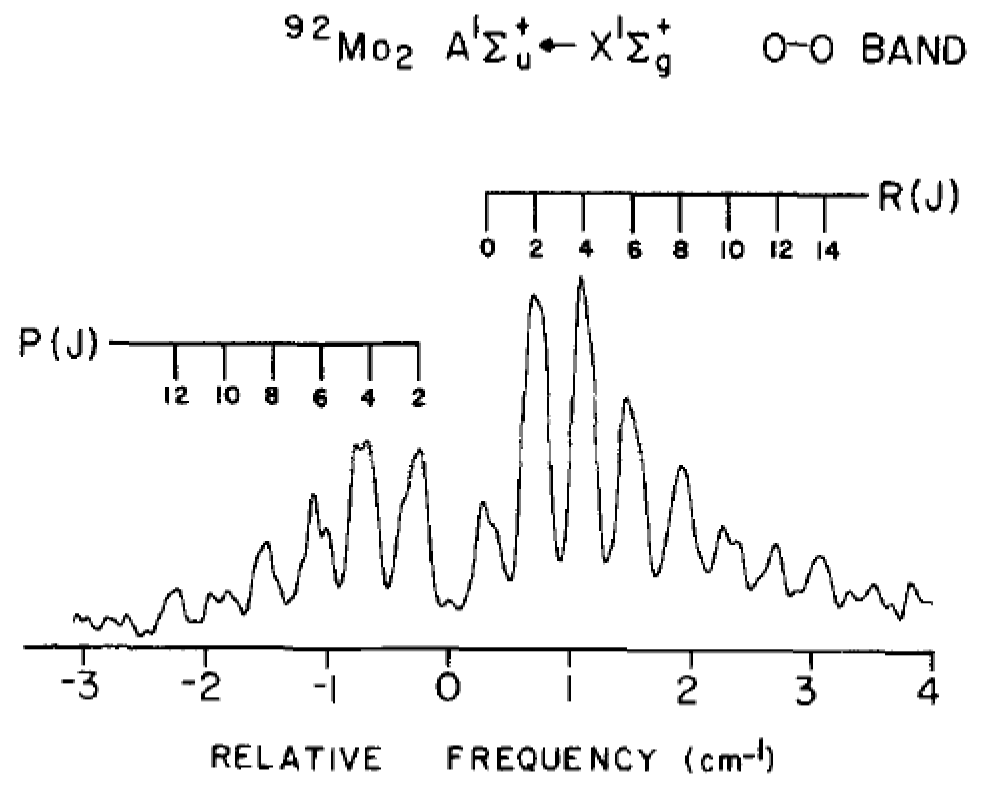

FIG. 8. High resolution spectra of the Mg_2 *A*–*X* (0–0) band. The intensity of $^{92}Mo_2^+$ photoions is plotted against the frequency of a scanning dye laser (bandwidth ~ 0.07 cm^{-1}, fluence ~ 15 $\mu J/cm^2$). Photoions of $^{92}Mo_2$ were created by absorption of one dye laser photon resonant with the *A*–*X* transition and one photon from the Nd : YAG fourth harmonic (266 nm, ~ 1 mJ/cm^2). Nozzle backing pressure was 8 atm.

Free Iron Clusters React Readily with O_2 and H_2S but Are Inert toward Methane

R. L. Whetten,* D. M. Cox, D. J. Trevor, and A. Kaldor

J. Phys. Chem. **1985**, *89*, 566–569

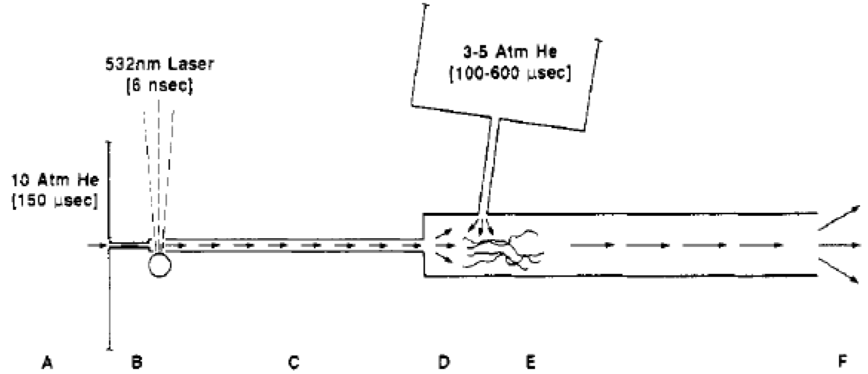

Figure 1. Scale-drawn schematic of essential features of the cluster source and chemical reactor. From left to right the method works as follows: (A) The primary nozzle opens for ≈150 μs and He expands from 10-atm stagnation pressure into a 1-mm-diameter channel. (B) At the peak of the primary He pulse, a focussed frequency-doubled Nd:YAG laser (20 mJ/pulse) strikes a rotating–translating Fe rod positioned where the 1-mm channel opens to 2 mm. (C) Sputtered metal atom vapor rapidly condenses and cools while flowing in the condensation channel; clusters approach the He velocity and arrive in a packet at the end of this channel. (D) The primary He pulse and clusters expand into the 1.1-cm-diameter reactor; the leading edge of this primary He pulse has swept out all secondary-pulse He and reactant to this point. (E) The secondary nozzle opens at a variable time with respect to the primary nozzle and laser, and the resulting expansion across the primary stream creates a turbulent zone of intimate mixing; this is the reaction zone, extending downstream toward the end of the reactor. (F) The mixed flow expands into vacuum (~10^{-6} torr), and a portion is collimated by a 5-mm conical skimmer into a molecular beam, where clusters and products are detected through photoionization mass spectrometry.

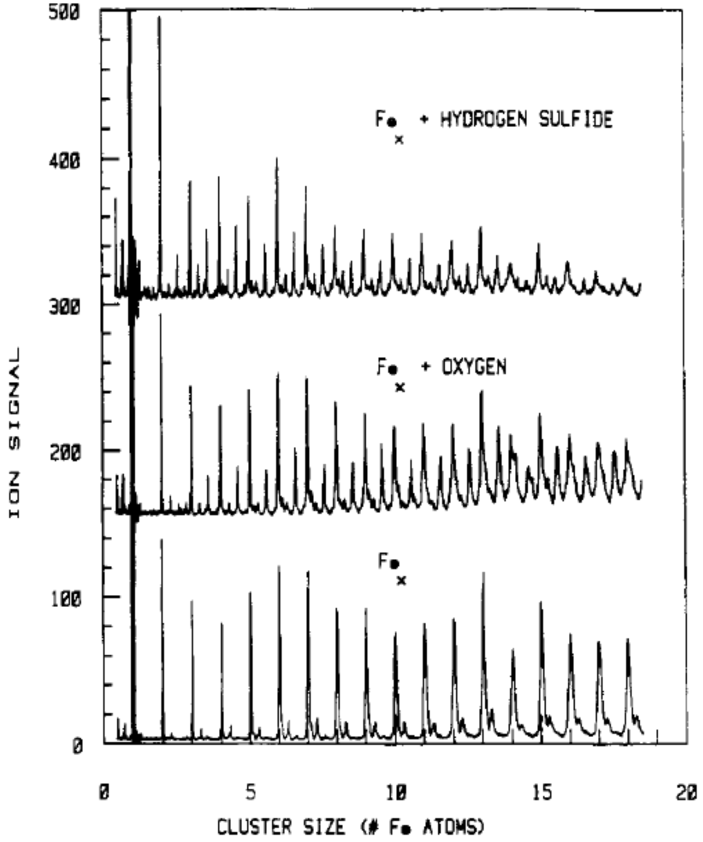

Figure 2. Examples of photoionization time-of-flight mass spectra of Fe clusters and the products of elementary reactions between these clusters and H_2S or O_2. Each trace is obtained with a 0.25-mJ laser pulse of 6.4-eV photons from an ArF laser focussed with a 25-cm cylindrical lens to a beam size of 1.5 cm by 0.03 cm. The bottom trace shows the free Fe cluster distribution obtained when the secondary nozzle is fired after the clusters pass; an identical distribution, although of 0.2–0.6 the intensity, is found when the secondary pulse of pure He overlaps the primary pulse. The small peaks just to the right of each cluster are Fe_xO clusters formed by co-condensation of Fe and impurity O atoms within the vaporization zone. The middle and upper traces show typical results obtained when 300–1000-ppm H_2S or O_2/He secondary pulses overlap the primary pulse. The strong new peaks all have masses corresponding to Fe_xS or Fe_xO_2 within ±1 amu for $x \leq 10$.

Surface reactions of metal clusters. II. Reactivity surveys with D2, N2, and CO

M. D. Morse, M. E. Geusic, J. R. Heath, and R. E. Smalley

Citation: The Journal of Chemical Physics **83**, 2293 (1985); doi: 10.1063/1.449321

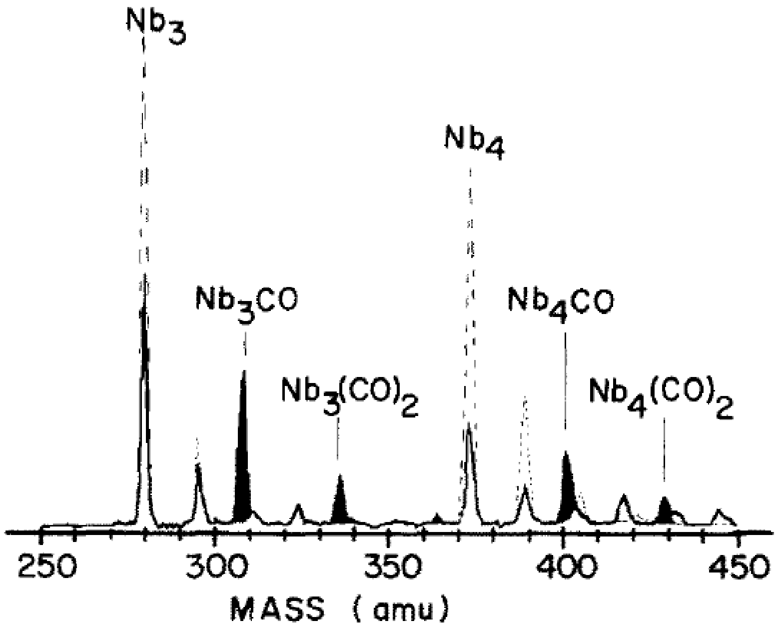

FIG. 1. Reaction study of small niobium clusters with CO. The dashed mass spectrum is that of the control experiment where only pure helium was injected into the reaction tube. The solid trace was observed when 2.4 sccm (cm^3 atm/min) of CO was injected (with a pure helium carrier) into the reaction tube. The features growing in due to formation of $Nb_n(CO)_m$ reaction products are blackened for emphasis. Corresponding reaction products for the Nb_nO cluster oxides are observable as small peaks on the base line.

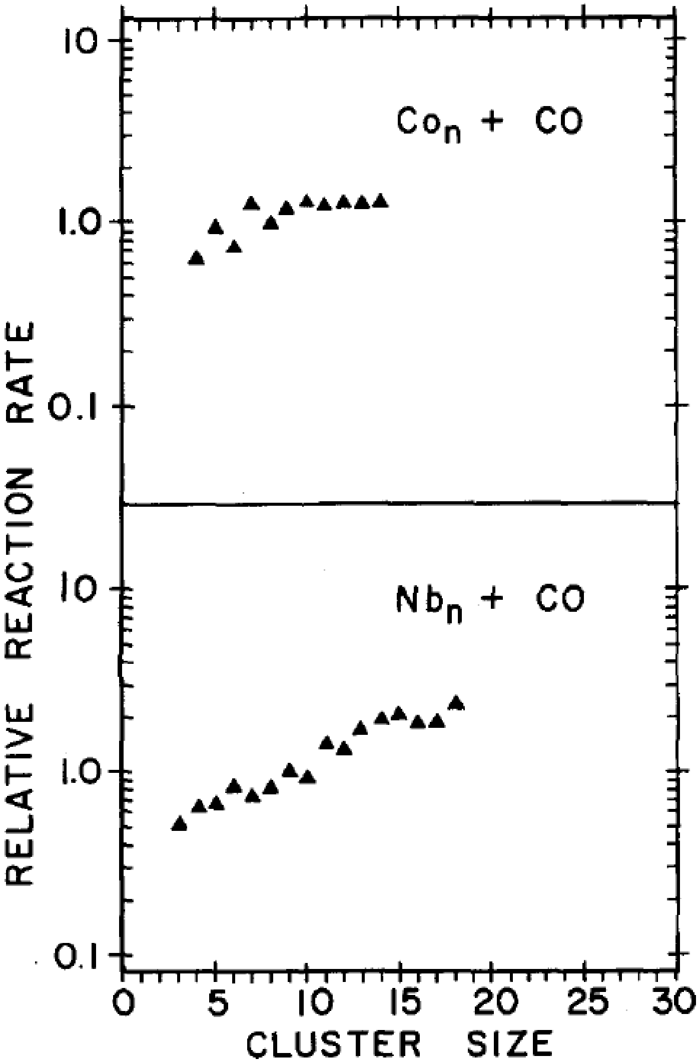

FIG. 2. Relative reaction rates for CO chemisorption for cobalt and niobium clusters. Estimated error bounds for these relative rate measurements are ±20%.

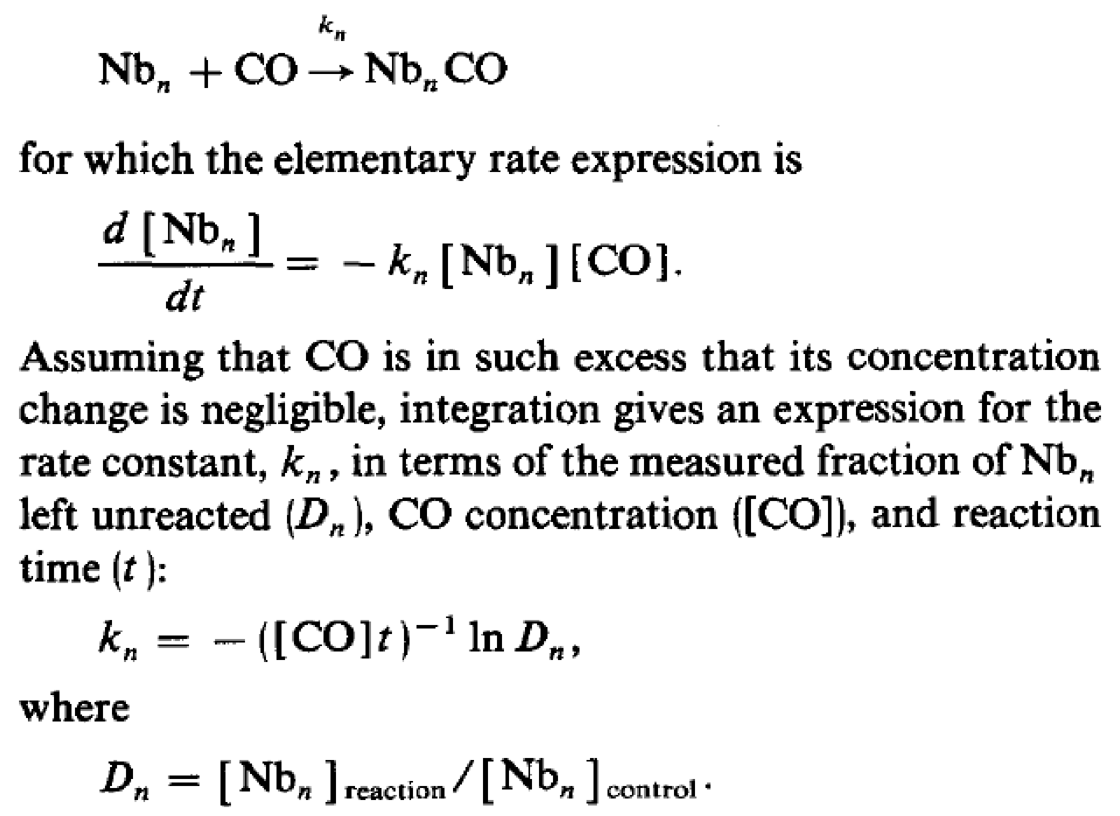

$$\mathrm{Nb}_n + \mathrm{CO} \xrightarrow{k_n} \mathrm{Nb}_n\mathrm{CO}$$

for which the elementary rate expression is

$$\frac{d\,[\mathrm{Nb}_n]}{dt} = -\,k_n\,[\mathrm{Nb}_n]\,[\mathrm{CO}].$$

Assuming that CO is in such excess that its concentration change is negligible, integration gives an expression for the rate constant, k_n, in terms of the measured fraction of Nb_n left unreacted (D_n), CO concentration ([CO]), and reaction time (t):

$$k_n = -\,([\mathrm{CO}]\,t)^{-1}\ln D_n,$$

where

$$D_n = [\mathrm{Nb}_n]_{\mathrm{reaction}}/[\mathrm{Nb}_n]_{\mathrm{control}}.$$

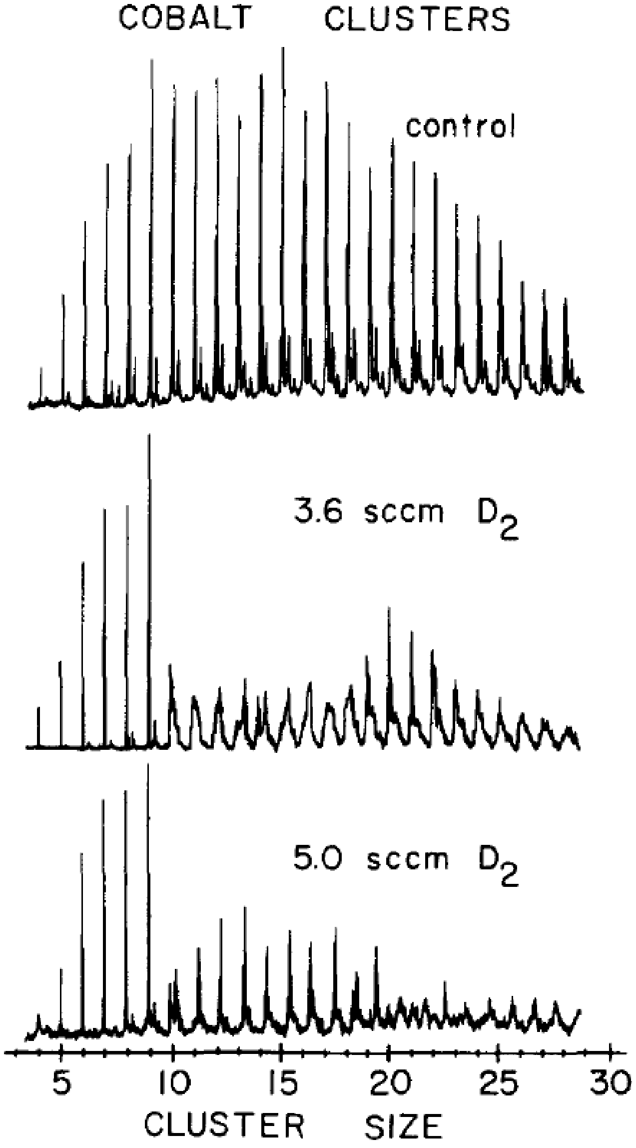

FIG. 3. Chemisorption study of D_2 on cobalt clusters. The control mass spectrum was performed with only pure helium injected as the reactant gas. The lower two mass spectra were taken with 3.6 and 5.0 sccm flow of injected D_2 reactant, respectively. See Figs. 4 and 5 for closer detail. The sharp peaks see in the bottom-most trace for clusters with more than 10 atoms are all due to cobalt clusters with more than one molecule of D_2 chemisorbed.

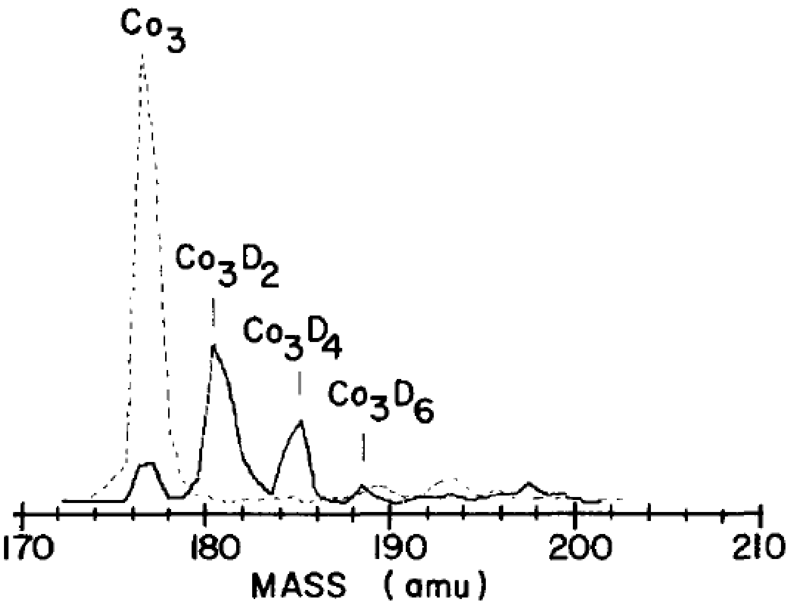

FIG. 4. Detail of the D_2 chemisorption experiment on Co trimer. The dashed mass spectrum is the control experiment (only pure helium as the reactant), the solid trace is the observed mass spectrum with an average reactant flow of 7.4 sccm D_2. Note that only reaction products with even numbers of deuterium atoms are observed. Careful examination of the base line reveal that the Co_3C carbide and Co_3O oxide which are produced in small amounts in the laser plasma of the cluster source also chemisorb D_2 strongly.

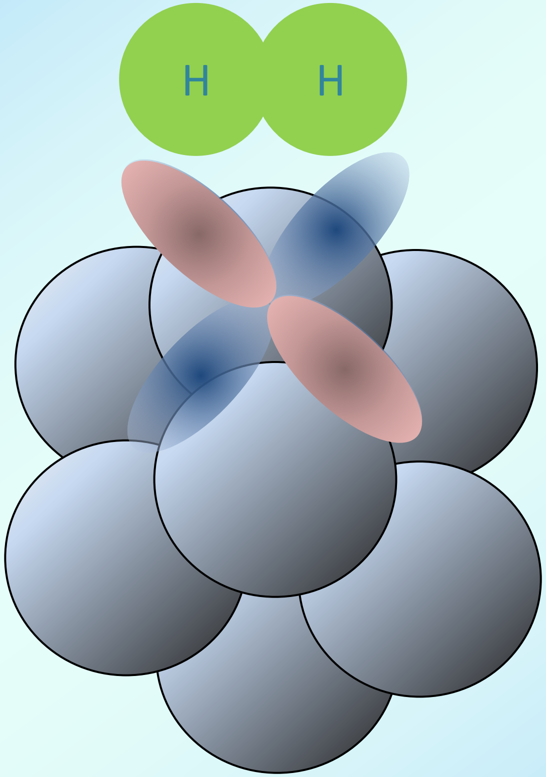

遷移金属元素
d軌道を持つ

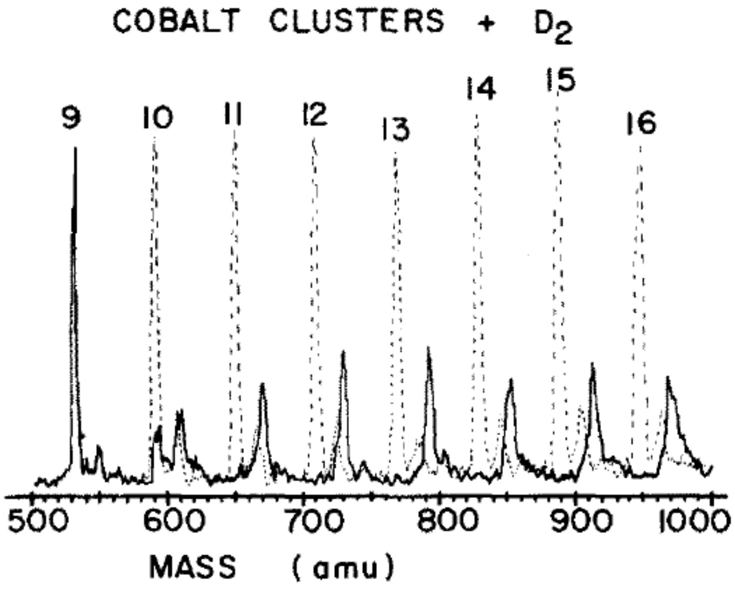

FIG. 5. Detail of D_2 chemisorption experiment in the 9–16 atom cluster range showing evidence for titration behavior in the chemisorption reaction. The dashed mass spectrum corresponds to the pure helium control experiment, the solid trace to a flow of 5.0 sccm D_2 injected into the reaction tube. The D_2 chemisorption process appears to shut off at five molecules of D_2 for Co_{11} and Co_{12}, six for Co_{13} and Co_{14}, and seven for Co_{15} and Co_{16}.

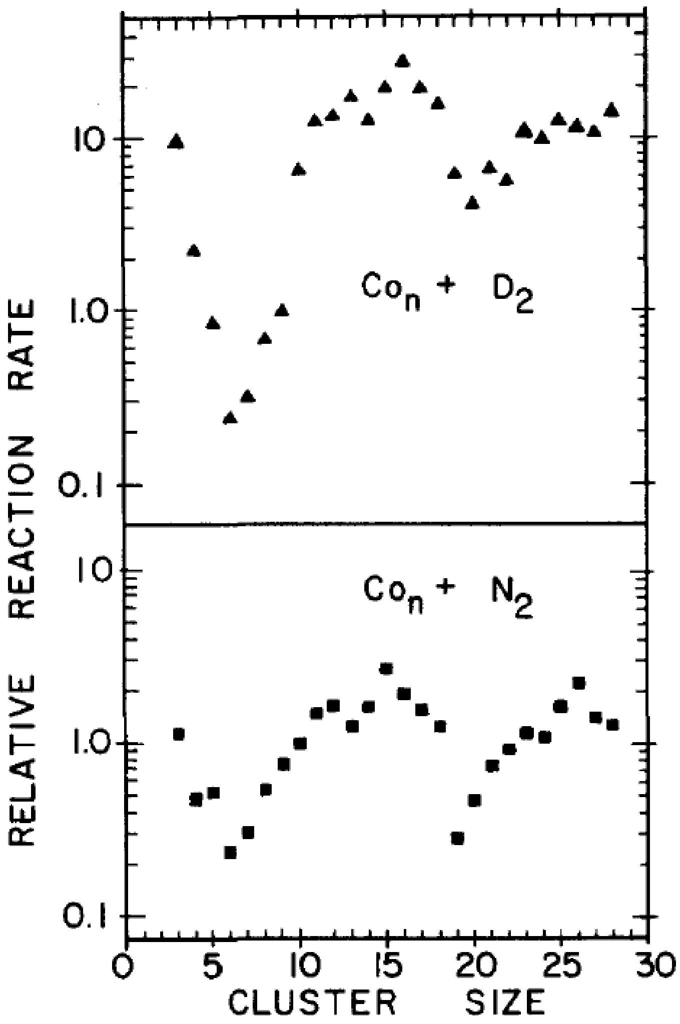

FIG. 7. Relative reaction rates of cobalt clusters with D_2 and N_2. Note the striking similarity in the reactivity patterns for these two reactants. The estimated errors for these relative rates is ± 20% except for rates greater than 10 or less than 0.1 compared to the reference rate; for these extreme rates the measurements are only of semiquantitative significance.

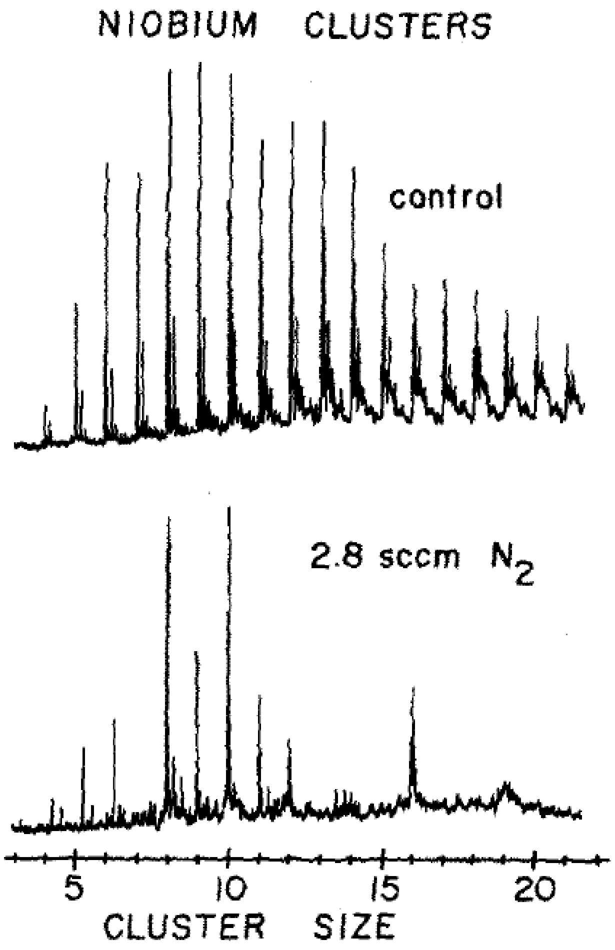

FIG. 9. Chemisorption study of N_2 on niobium clusters. The sharp peaks in the small cluster region of the lower mass spectrum are due to the N_2 chemisorption product, whereas the peaks seen in roughly the correct position for the 8–12 and 16th cluster of niobium are, in fact, due to the unreacted bare cluster.

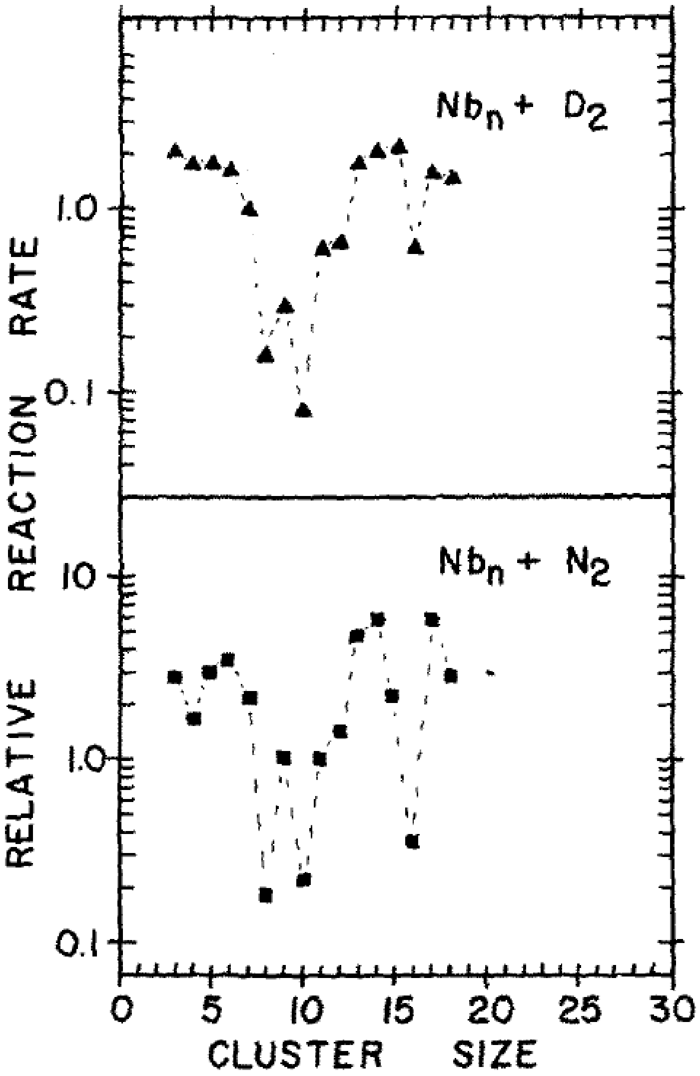

FIG. 11. Relative reaction rates of niobium clusters with D_2 and N_2. Note the similarity in the reactivity patterns for these two reactants. Estimated error bounds for these relative rates are ± 20% except for the extremely low and high reactivity points which are only semiquantitative.

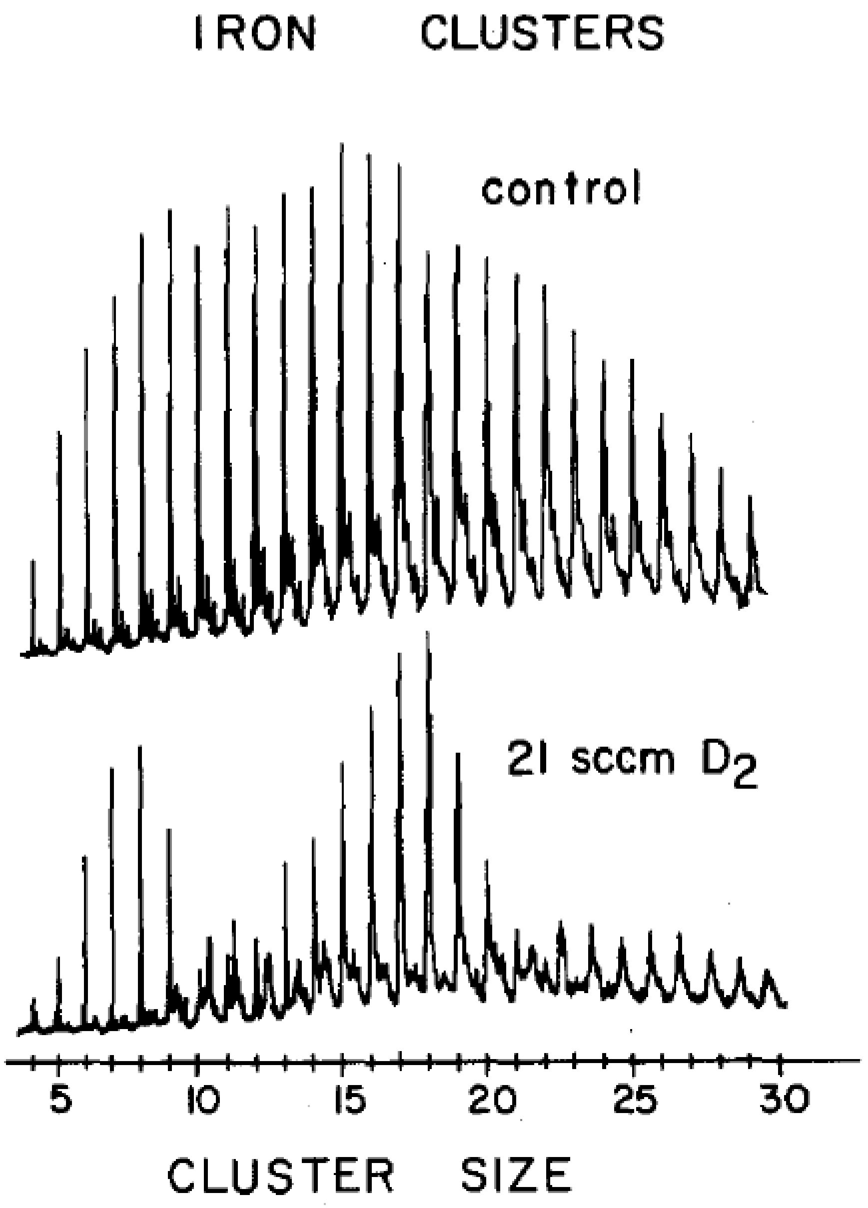

FIG. 14. Chemisorption study of D_2 on iron clusters.

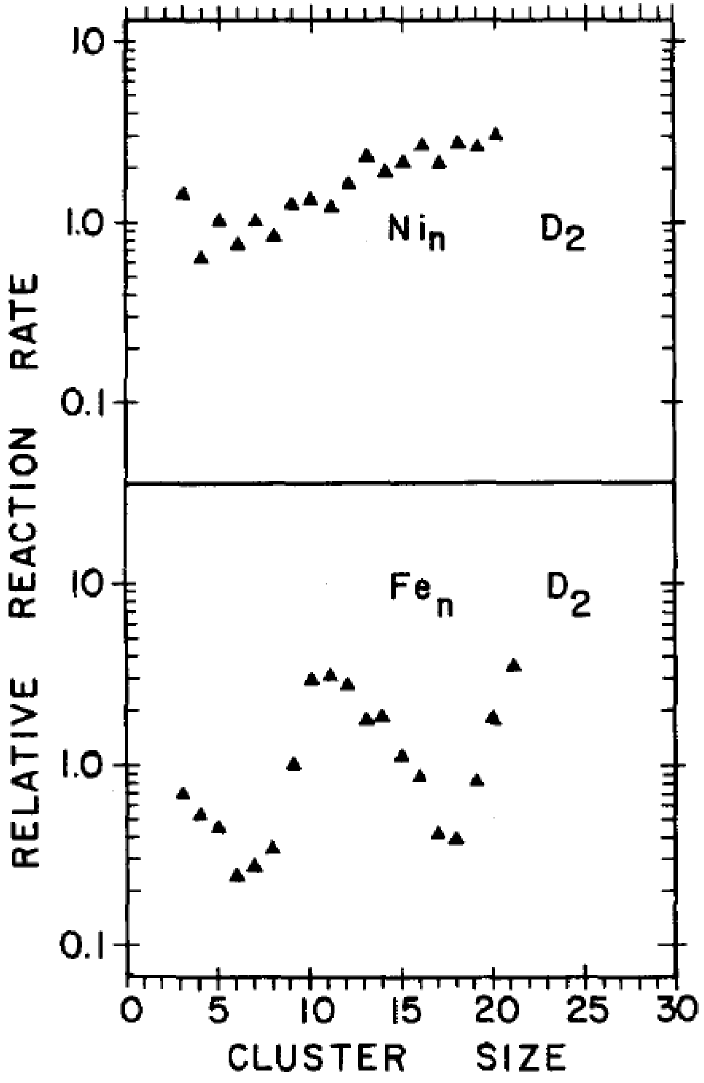

FIG. 15. Relative reaction rates for nickel and iron chemisorption rates with D_2.

Gas phase reactions of iron clusters with hydrogen. I. Kinetics

S. C. Richtsmeier, E. K. Parks, K. Liu, L. G. Pobo, and S. J. Riley

The Journal of Chemical Physics **82**, 3659 (1985)

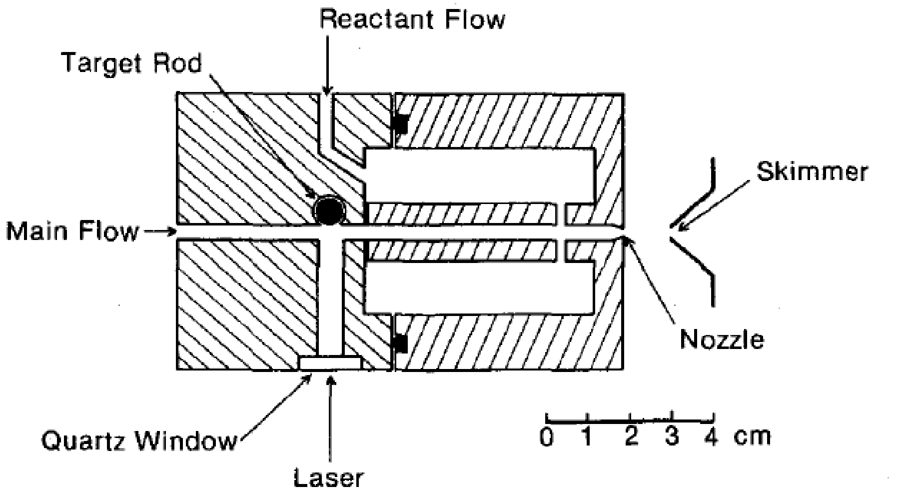

FIG. 1. Cross sectional view of the laser vaporization cluster source/flow tube reactor.

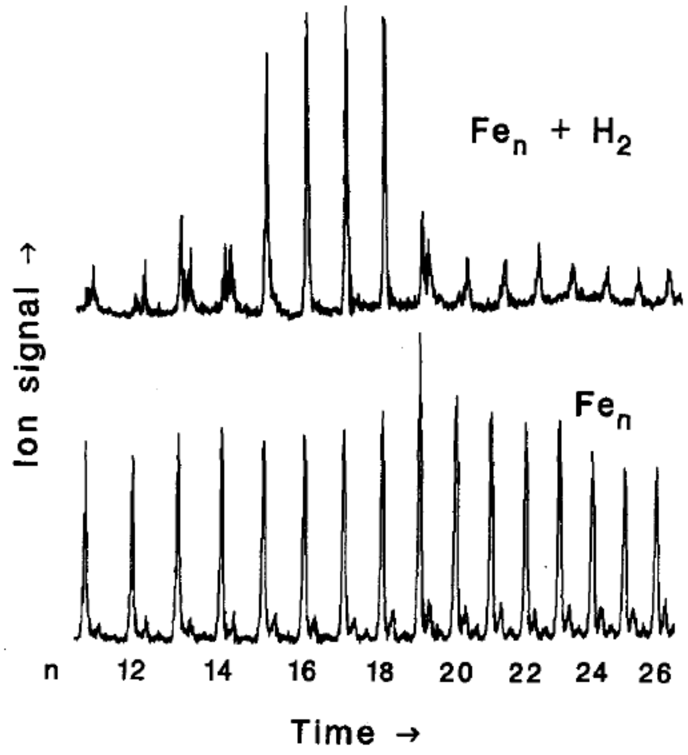

FIG. 2. A portion of the cluster time-of-flight mass spectrum showing Fe_{11} to Fe_{26} species. The lower panel is the bare cluster signal (no reagent gas). Satellite peaks are impurities, mostly cluster oxides and dioxides. For the upper panel, 7 sccm of H_2 was added to the reagent line. Note the small extent of reaction shown by Fe_{15} through Fe_{18}, and the varying degrees of reaction for the other clusters.

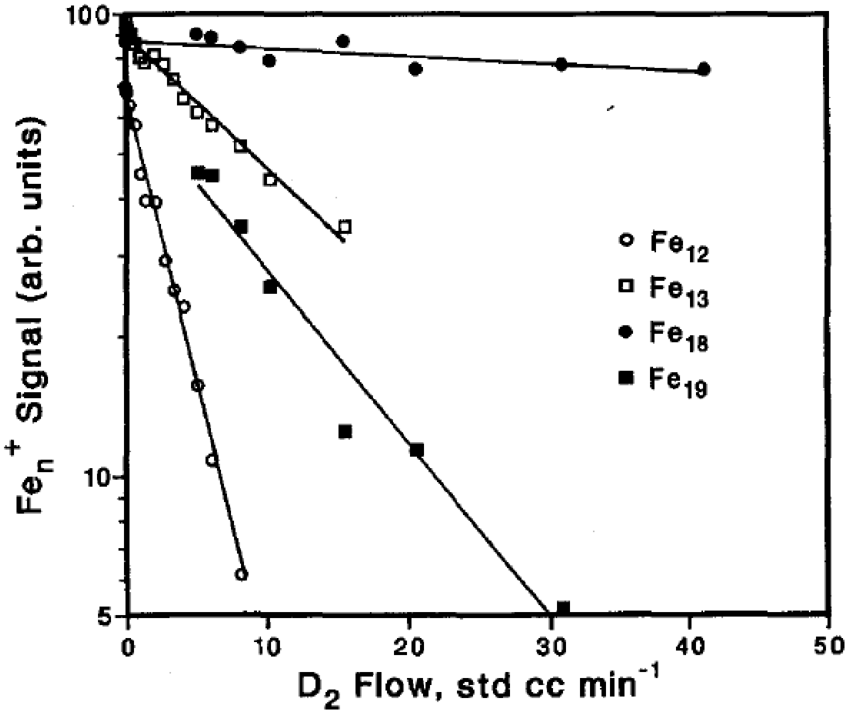

FIG. 3. Examples of the logarithmic relationship between unreacted bare cluster signal and D_2 flow. Data points are integrated intensities of the bare cluster peaks in the mass spectra. Lines are least squares fits to the points.

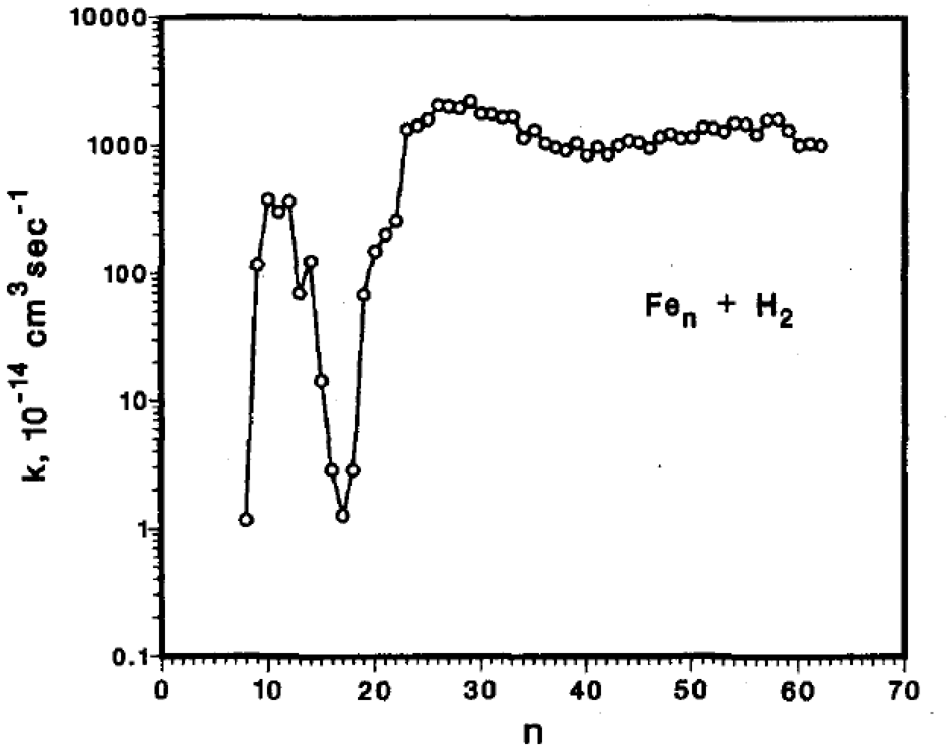

FIG. 4. Cluster size dependence of the rate constants for reaction with H_2. Data points were determined from the slopes of a series of plots similar to Fig. 3. For most experiments the buffer gas pressure was ~30 Torr.

Reactions of iron clusters with hydrogen. II. Composition of the fully hydrogenated products

E. K. Parks, K. Liu, S. C. Richtsmeier, L. G. Pobo, and S. J. Riley

The Journal of Chemical Physics **82**, 5470 (1985)

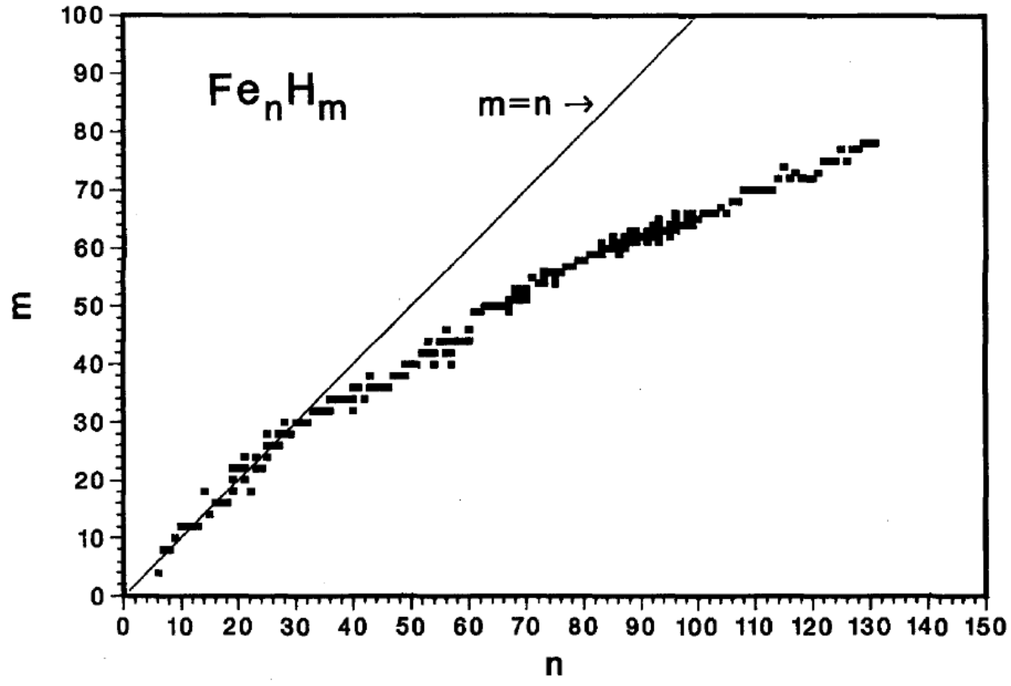

FIG. 1. Compositions of the cluster hydrides Fe_nH_m. For $n < 60$ the plotted symbols correspond to the hydrides that have appreciable intensity in the mass spectra. For $60 < n < 100$ the center of each symbol corresponds to the center of the observed mass peak (individual hydrides are not resolved above $n = 60$) and the height gives the range of m values that contribute to the peak. Above $n = 100$ only the peak center is indicated.

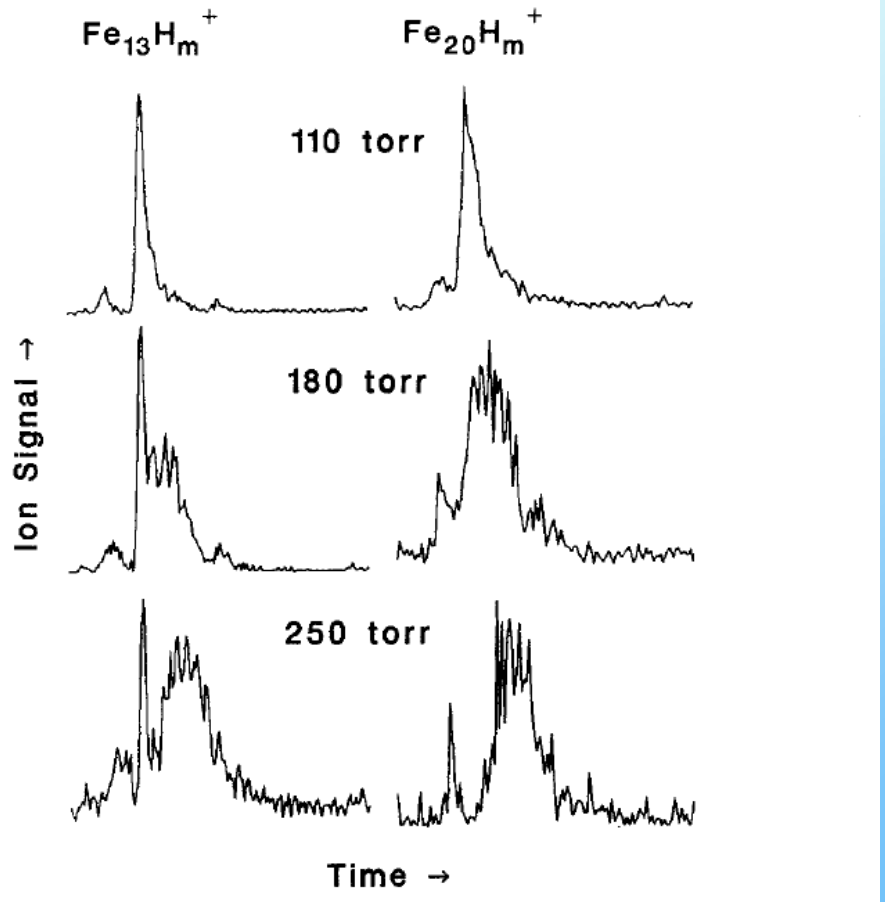

FIG. 2. Time-of-flight mass spectra of the hydrides of Fe_{13} and Fe_{20} showing the increasing hydrogenation that occurs at higher hydrogen pressures.

Reactions of iron clusters with hydrogen. III. Laser-induced desorption of H2 by multiphoton absorption

K. Liu, E. K. Parks, S. C. Richtsmeier, L. G. Pobo, and S. J. Riley

The Journal of Chemical Physics **83**, 2882 (1985)

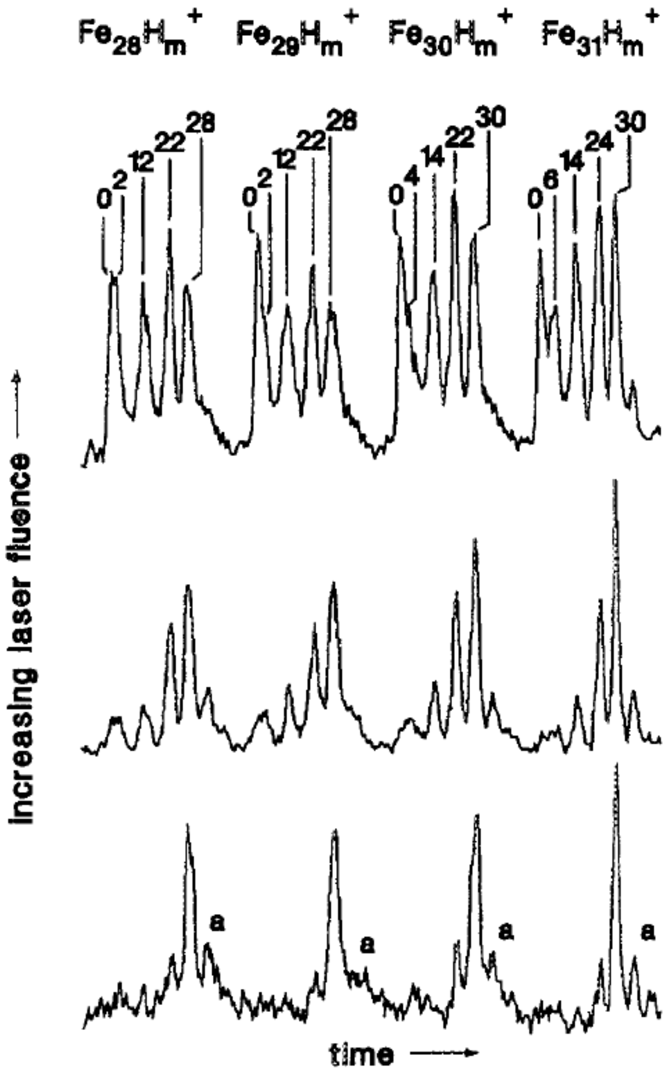

FIG. 1. A portion of the time-of-flight mass spectrum of hydrogenated iron clusters for three different ArF ionizing laser fluences. In the top spectrum the number of hydrogens in each of the identifiable hydride species is indicated. The peaks labeled "a" in the lowest spectrum are due to a small (1%) copper impurity in the iron target sample.

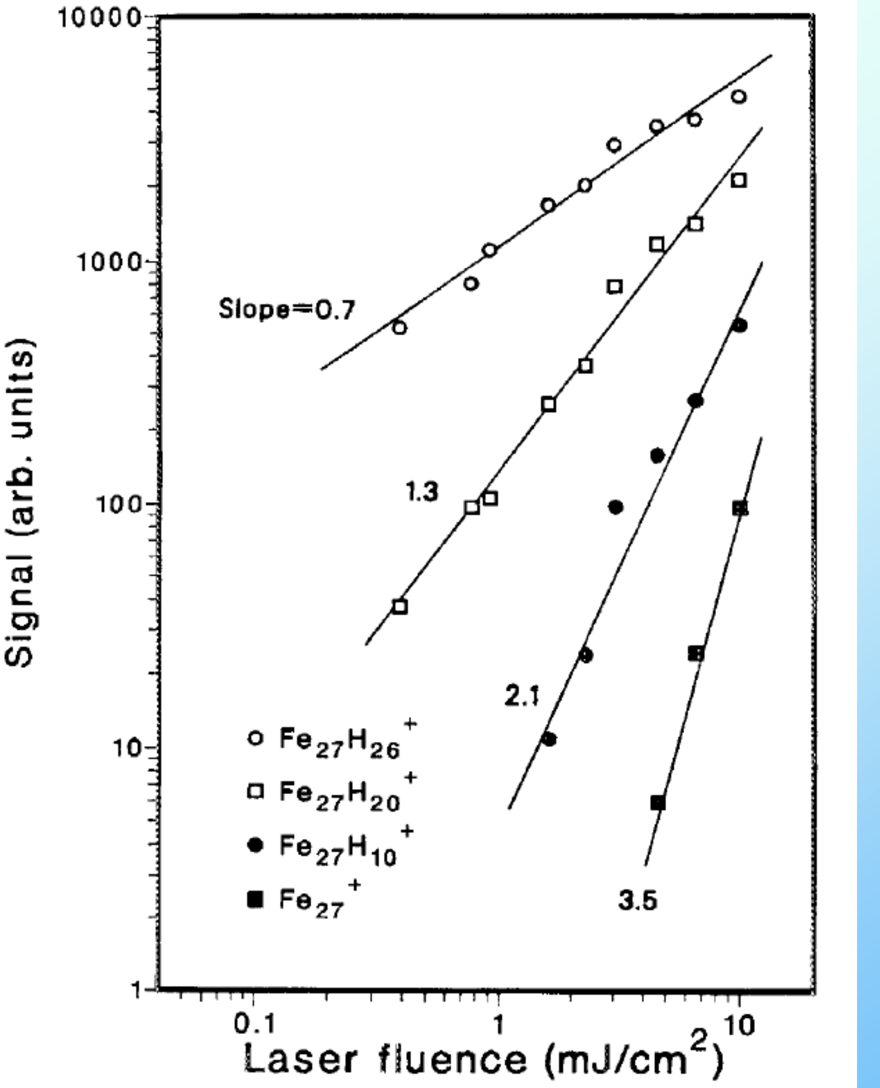

FIG. 2. Ionizing laser fluence dependence of the various species resulting from ionization and fragmentation of $Fe_{27}H_{26}$. The four sets of data are offset by arbitrary amounts for clarity.

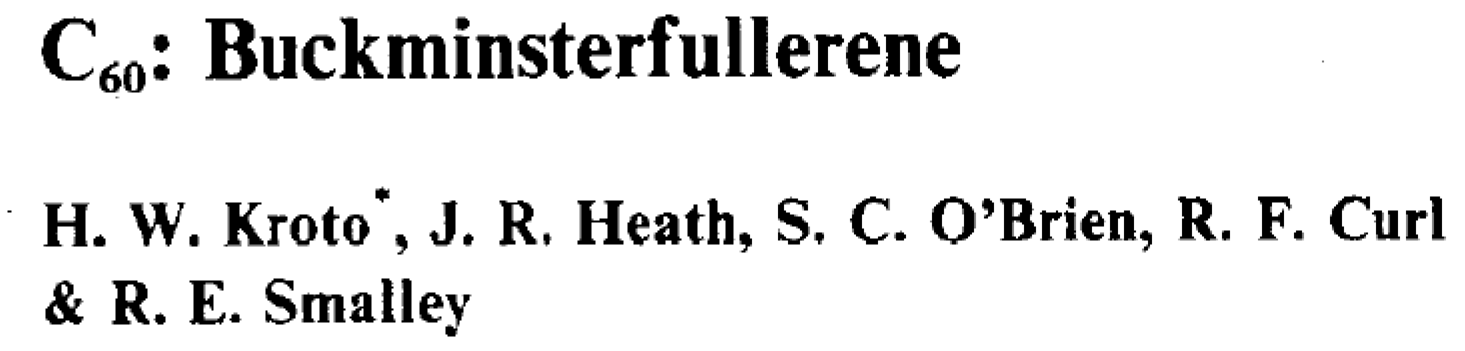

C_{60}: Buckminsterfullerene

H. W. Kroto*, J. R. Heath, S. C. O'Brien, R. F. Curl & R. E. Smalley

NATURE VOL. 318 14 NOVEMBER 1985

pp162-163

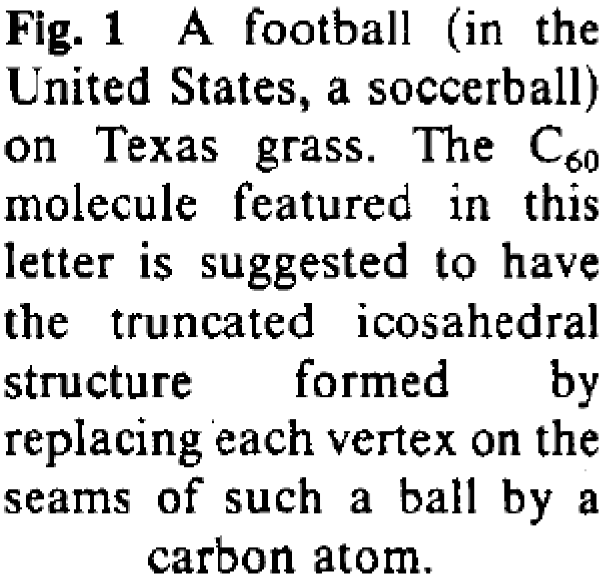

Fig. 1 A football (in the United States, a soccerball) on Texas grass. The C_{60} molecule featured in this letter is suggested to have the truncated icosahedral structure formed by replacing each vertex on the seams of such a ball by a carbon atom.

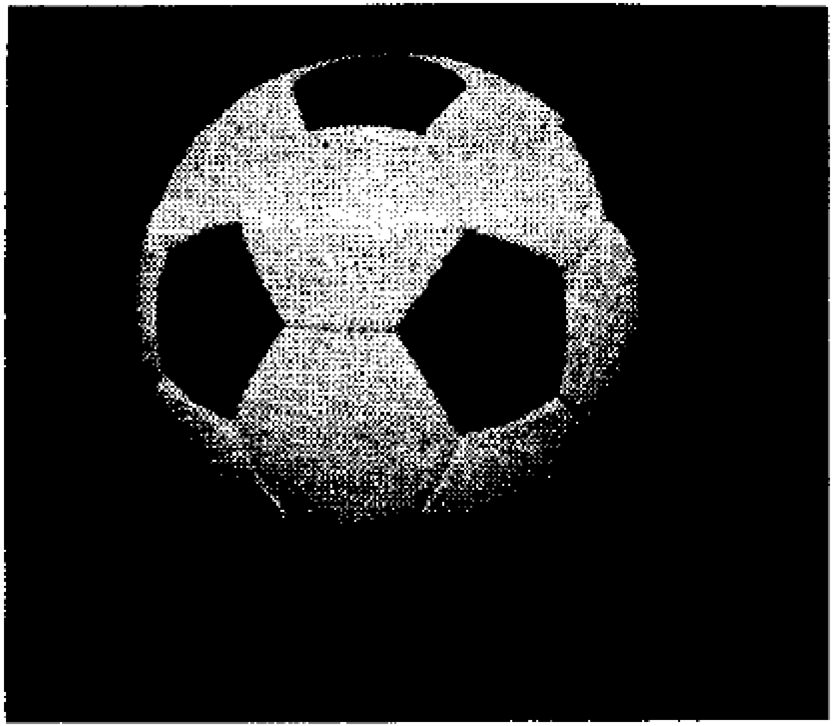

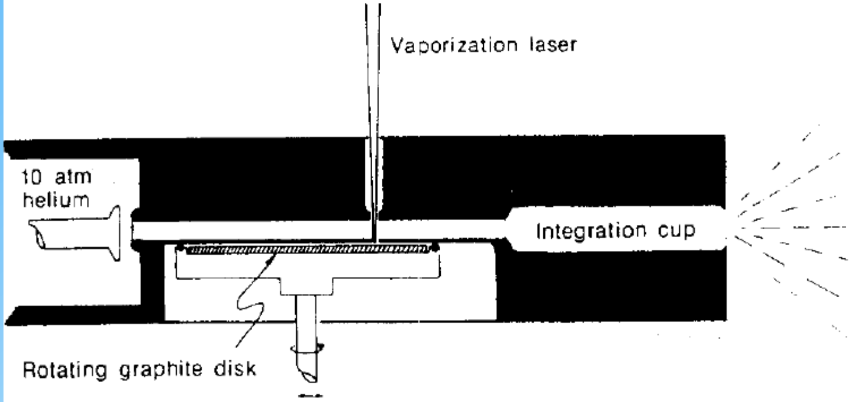

Fig. 2 Schematic diagram of the pulsed supersonic nozzle used to generate carbon cluster beams. The integrating cup can be

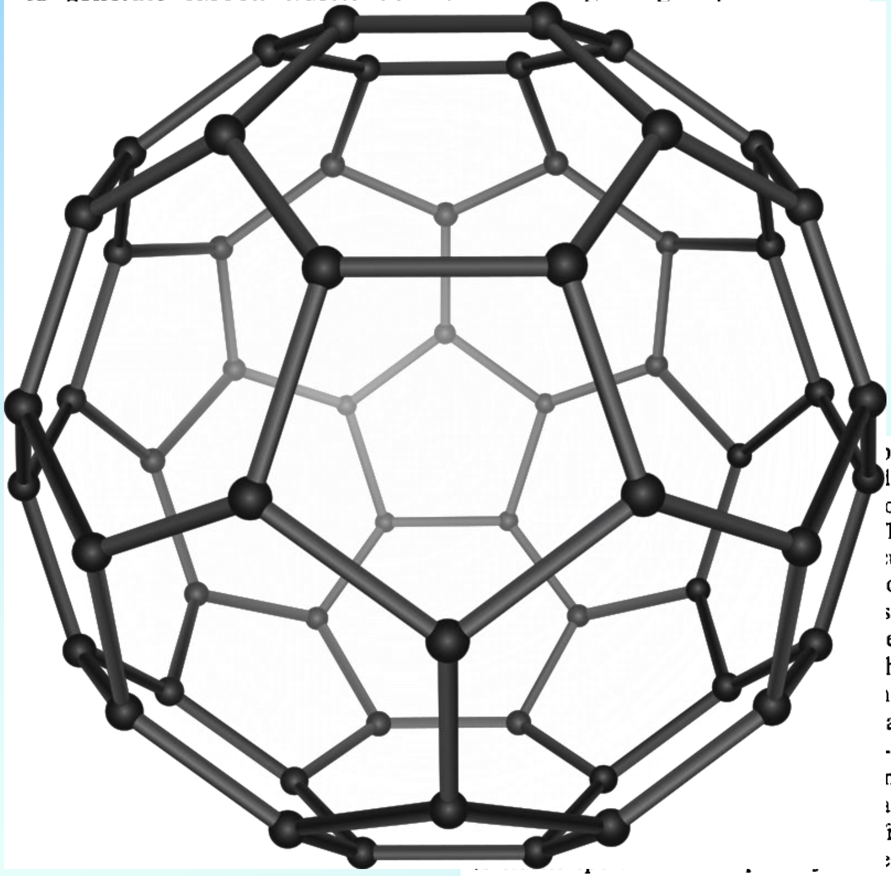

on clusters prepared by
l in a supersonic beam.
oton excitation with an
he three spectra shown
urring in the supersonic
over the graphite target
ster distribution here is
e graphite sheet ejected
he spectrum in *b* was
was present over the
ation. The enhancement
-phase reactions at these
m in *a* was obtained by
nd cluster-cluster reac-
ig. 2. The concentration
C_{60} form is the prime
experimental observation of this study.

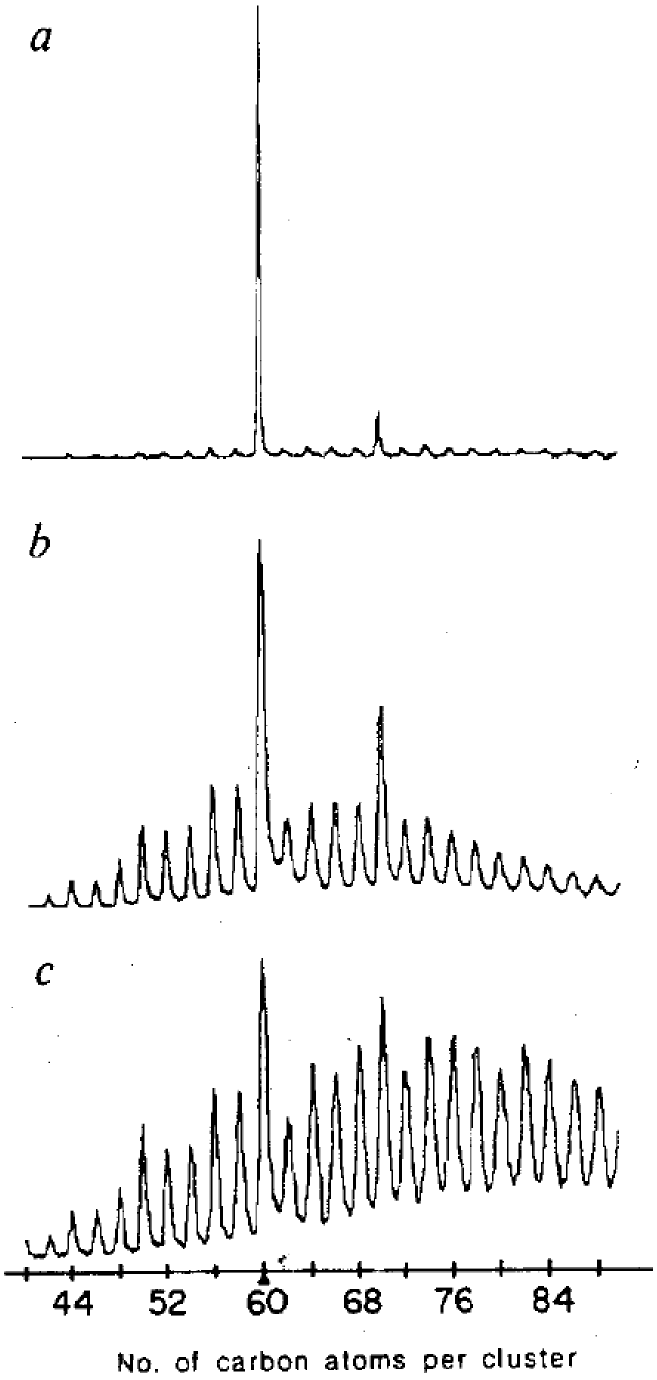

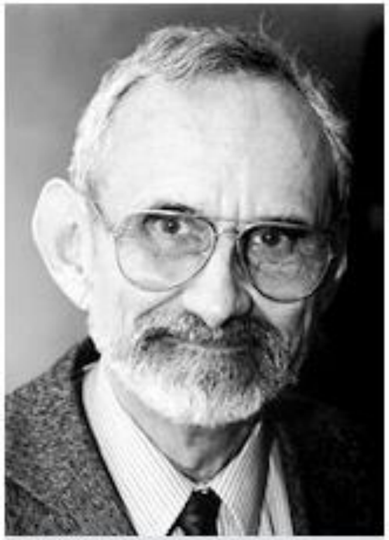

Robert F. Curl Jr.

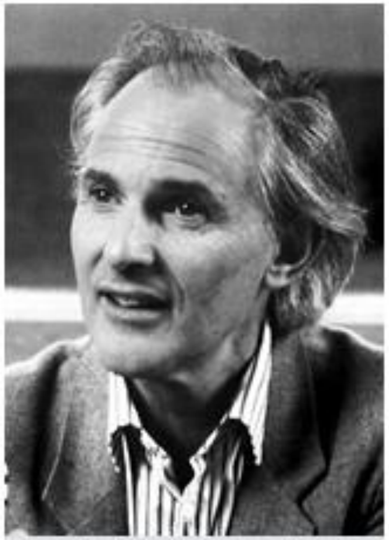

Sir Harold W. Kroto

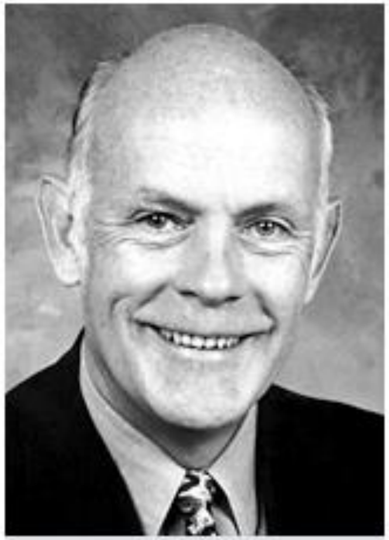

Richard E. Smalley

Bucky balls or Fullerenes were discovered by H.W.Kroto, R.F.Curt and R.E.Smalley. The 1996 Nobel Prize was awarded to above scientists for the discovery of fullerenes.

Structure and Reactivity of Bimetallic Co_nV_m Clusters

S. Nonose, Y. Sone, K. Onodera, S. Sudo, and K. Kaya

***J. Phys. Chem.* 1990, *94,* 2144-2146**

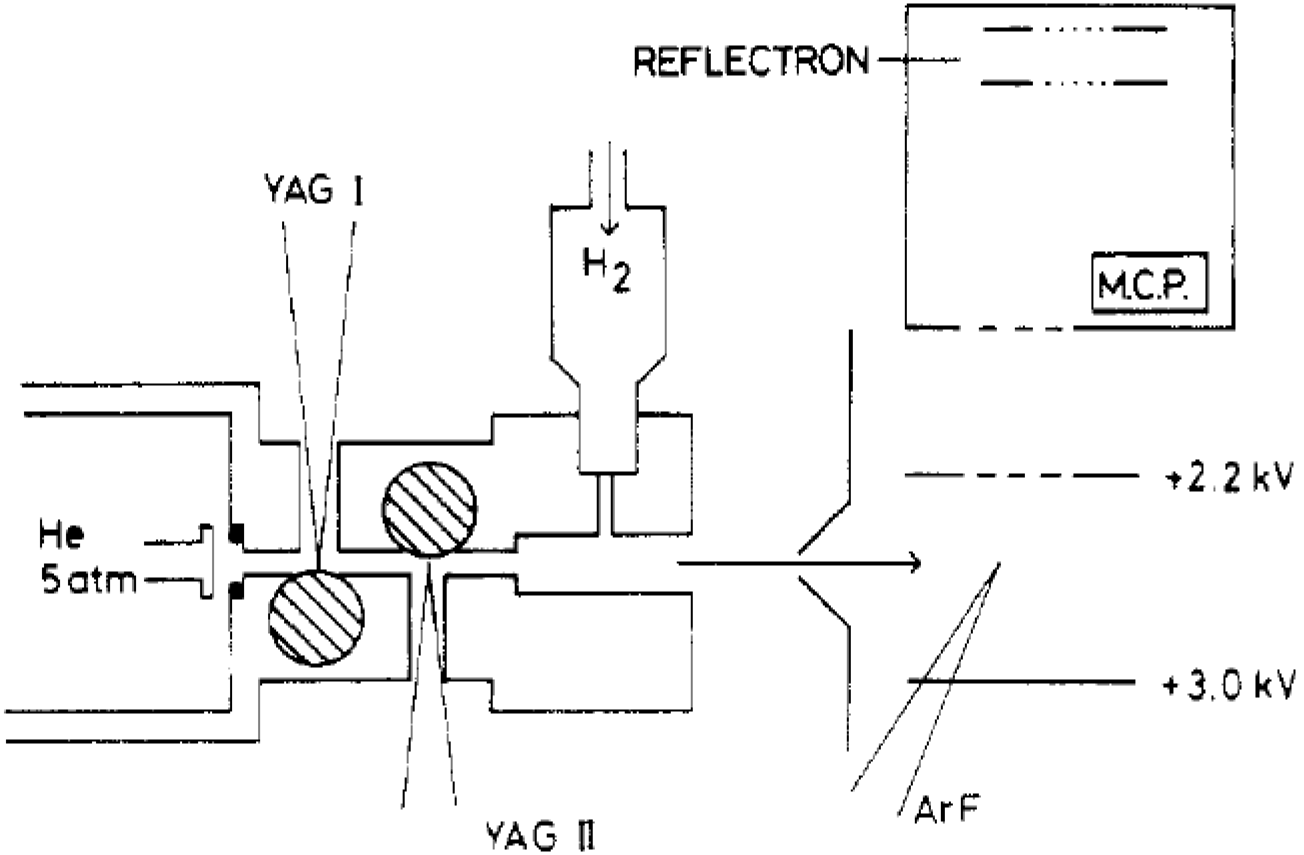

Figure 1. Schematic diagram of experimental apparatus. Clusters composed of two metal elements are synthesized via vaporization of two target rods by two pulsed YAG lasers. Chemical reactions are performed using a fast-flow reactor. The reaction products are ionized by ArF excimer laser and detected by a time-of-flight (TOF) mass spectrometer equipped with a reflectron.

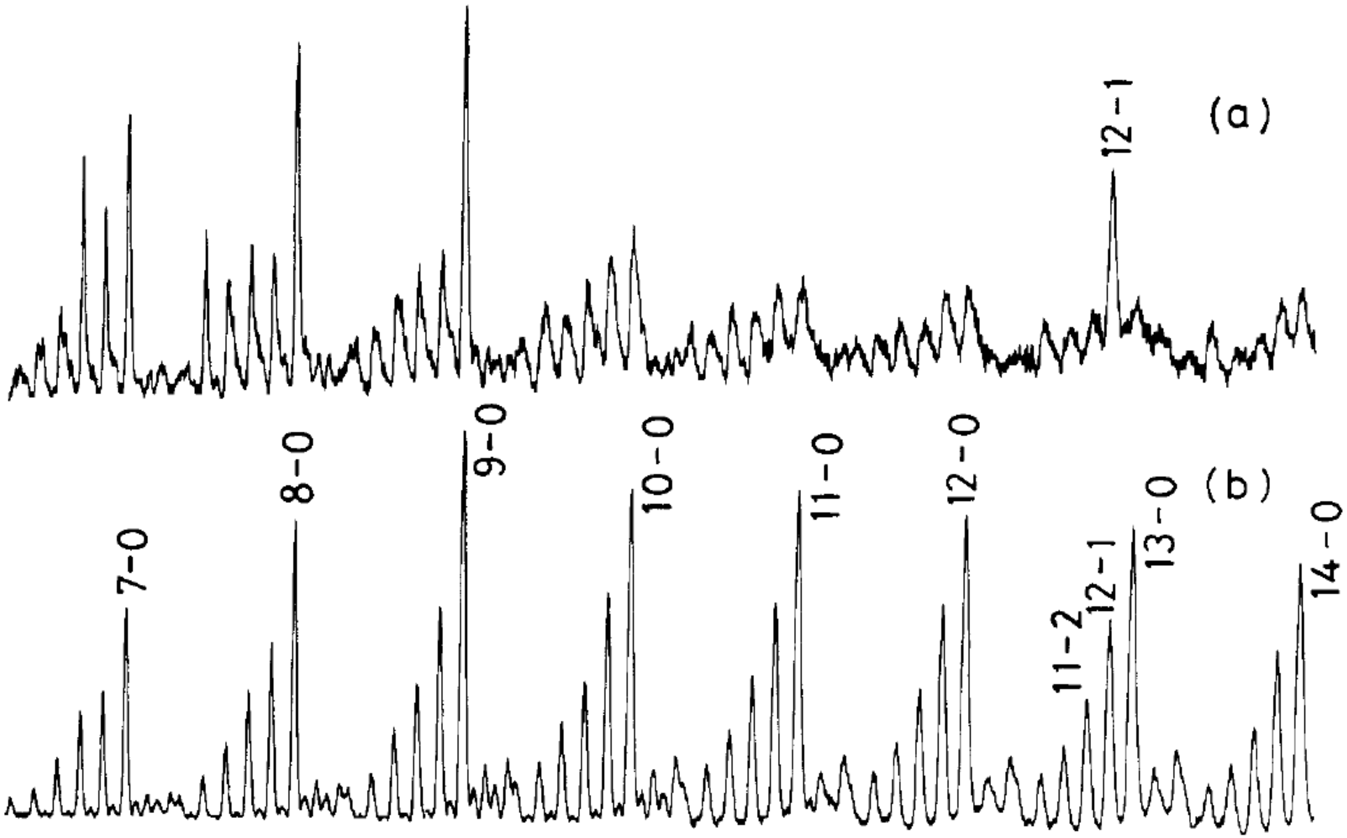

Figure 2. TOF mass spectra of $Co_{n-m}V_m$ ($n > m$) clusters (from $n = 7$ to 14) mixed with (a) 100 Torr of H_2 seeded in 1 atm of He and (b) only pure He as a reference. Peaks of the clusters are labeled according to the notation $n-m$, denoting the number of cobalt atoms (n) and substituted vanadium atoms (m).

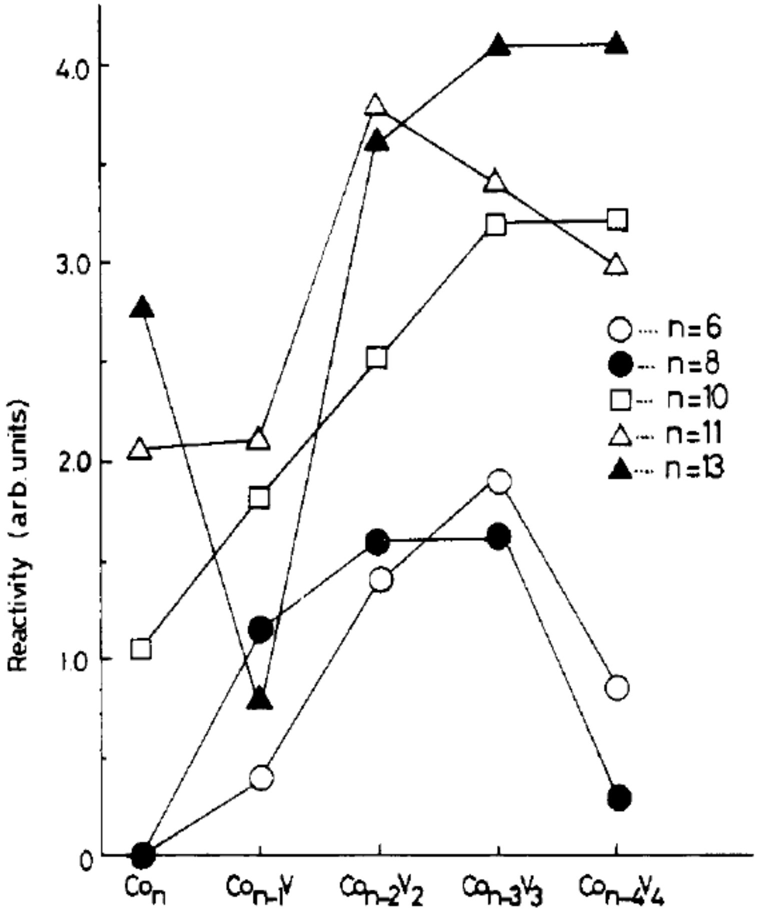

Figure 3. The relative rate constant R_n of $Co_{n-m}V_m$ $(n > m)$ clusters for reaction with H_2. Open circles, closed circles, open squares, open triangles, and closed triangles are R_n of n = 6, 8, 10, 11, and 13, respectively.

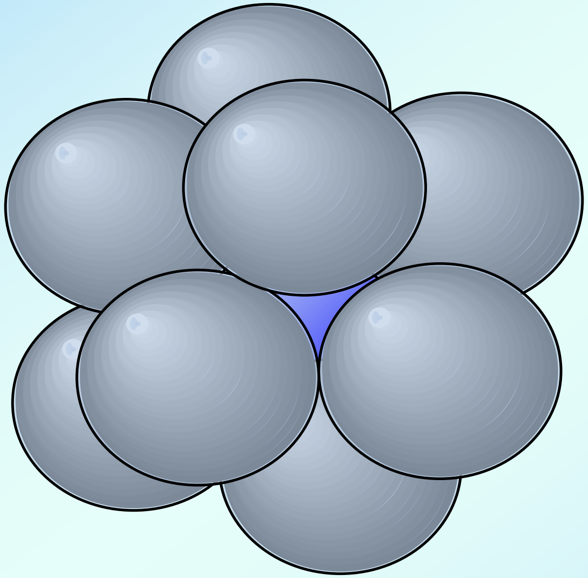

$Co_{12}V_1$

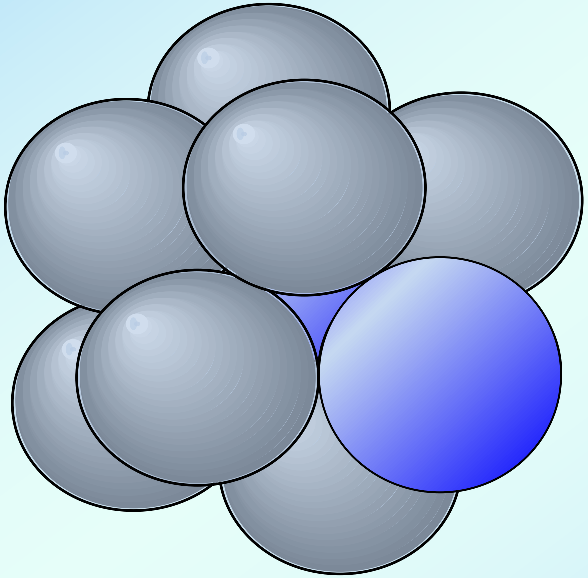

$Co_{11}V_2$

REACTIVITY STUDY OF ALLOY CLUSTERS MADE OF ALUMINUM AND SOME TRANSITION METALS WITH HYDROGEN

Shinji NONOSE, Yasutomo SONE, Ken ONODERA,
Shigeto SUDO and Koji KAYA

CHEMICAL PHYSICS LETTERS,
Volume 164, number 4, I5 December 1989

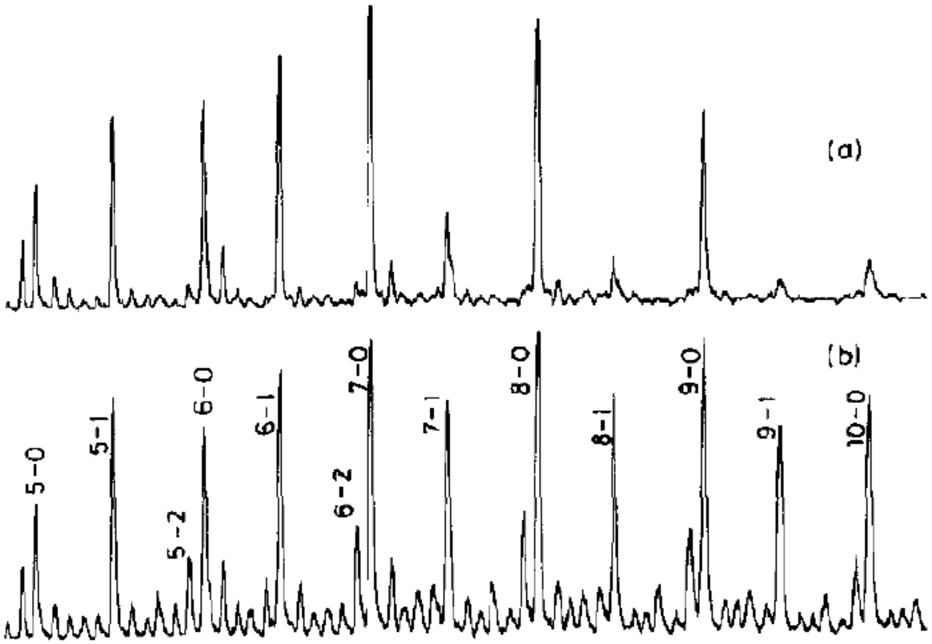

Fig. 1. TOF mass spectra of Co_nAl_m ($n > m$) clusters (from $n = 5$ to 10) reacted with (a) 100 Torr H_2 seeded in 1 atm He and (b) pure He as a reference. Peaks of the clusters are labelled according to the notation n–m, denoting the number of cobalt atoms (n) and aluminum atoms (m), respectively.

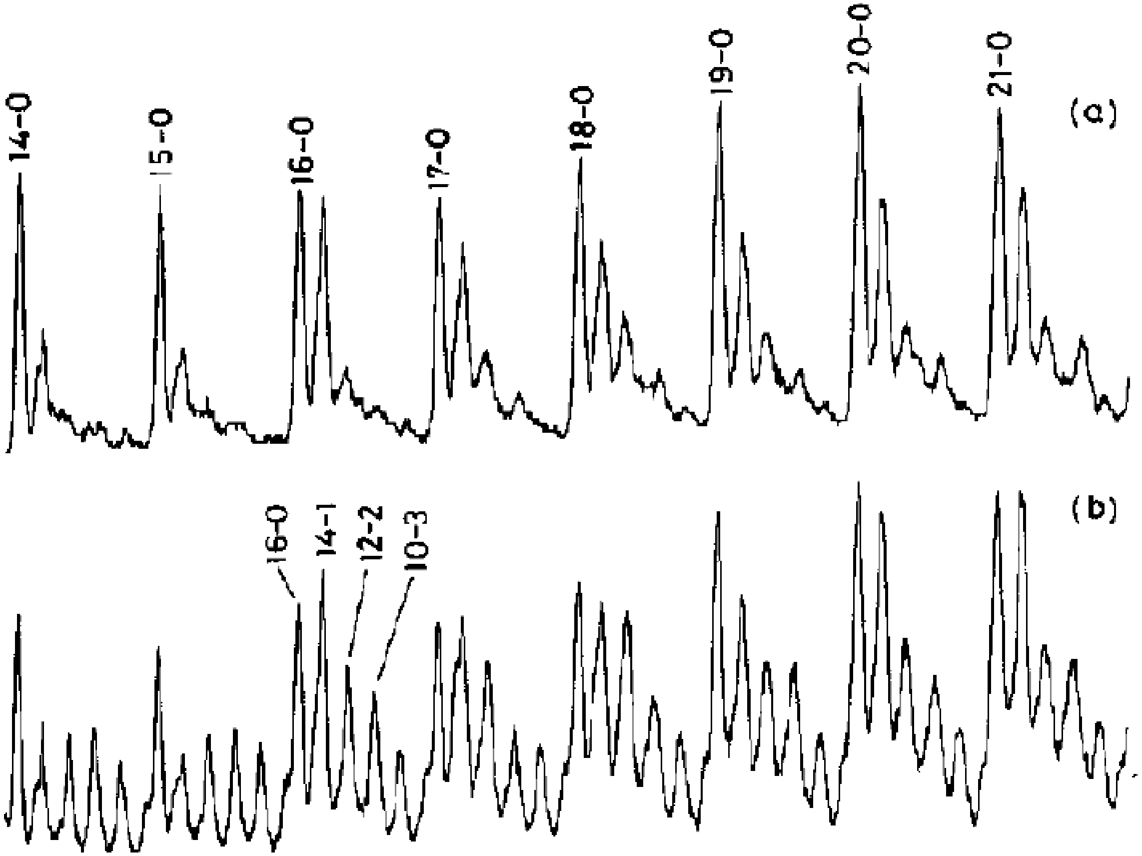

Fig. 2. TOF mass spectra of Al_nCo_m ($n>m$) clusters (from $n=14$ to 21) reacted with (a) H_2 and (b) He as a reference. Peaks of the clusters are labelled according to the notation n–m, denoting the number of aluminum atoms (n) and cobalt atoms (m), respectively.

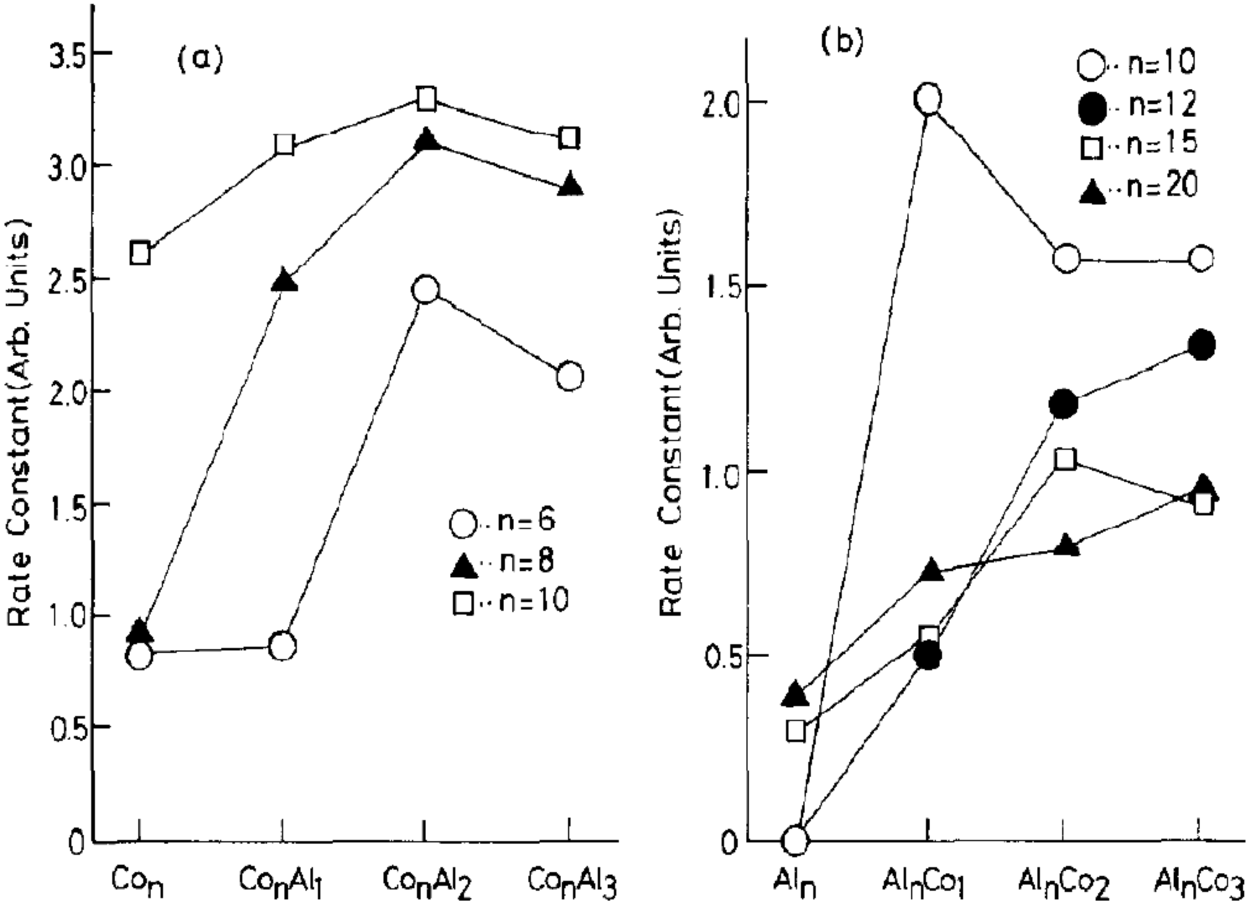

Fig. 3. (a) The relative rate constant R_n of Co_nAl_m ($n > m$) clusters for reaction with H_2 is plotted as a function of the number of aluminum atoms (from $m=0$ to 3). Open circles, closed triangles and open squares are R_n of Co_6Al_m, Co_8Al_m and $Co_{10}Al_m$, respectively. (b) The relative rate constant R_n of Al_nCo_m ($n > m$) clusters for reaction with H_2 is plotted as a function of the number of cobalt atoms (from $m=0$ to 3). Open circles, closed circles, open squares and closed triangles are R_n of $Al_{10}Co_m$, $Al_{12}Co_m$, $Al_{15}Co_m$ and $Al_{20}Co_m$, respectively.

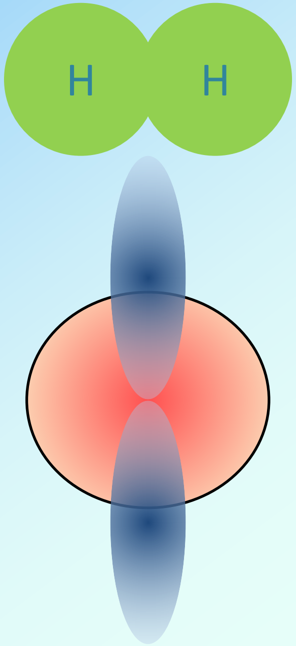

Al

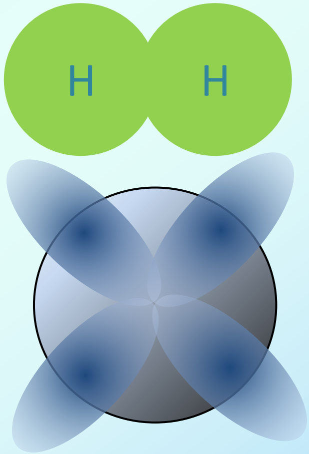

Co

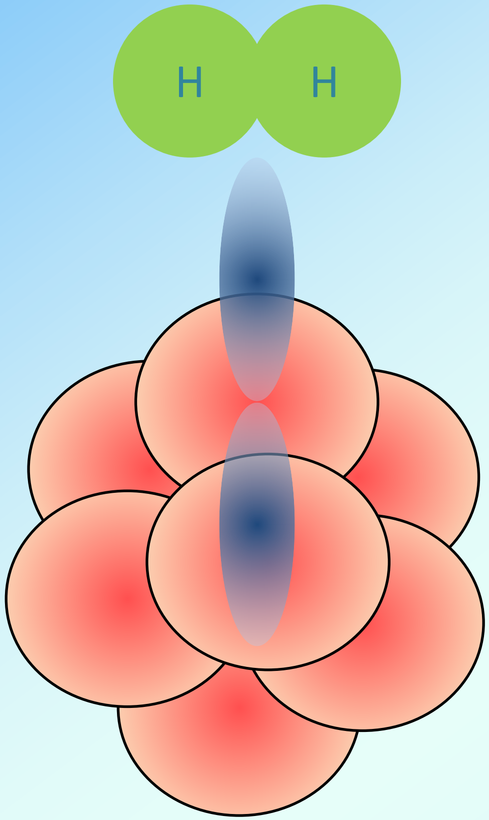

Al
典型金属元素
s,p軌道のみ

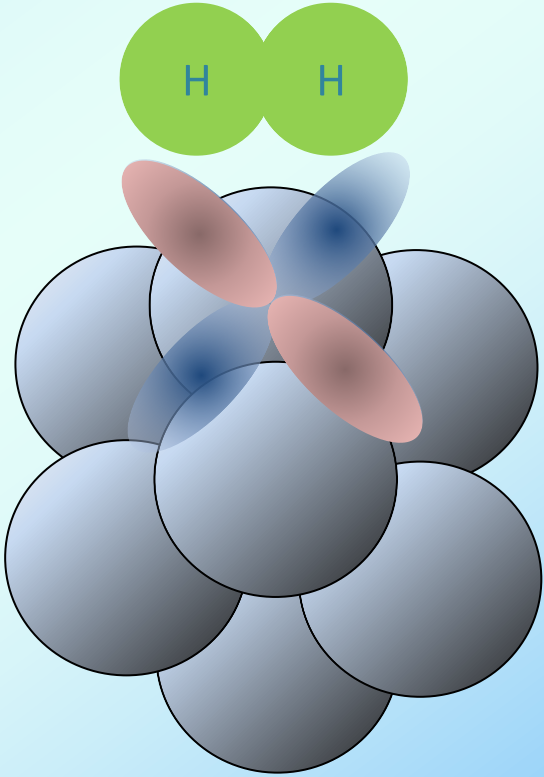

Co
遷移金属元素
d軌道を持つ

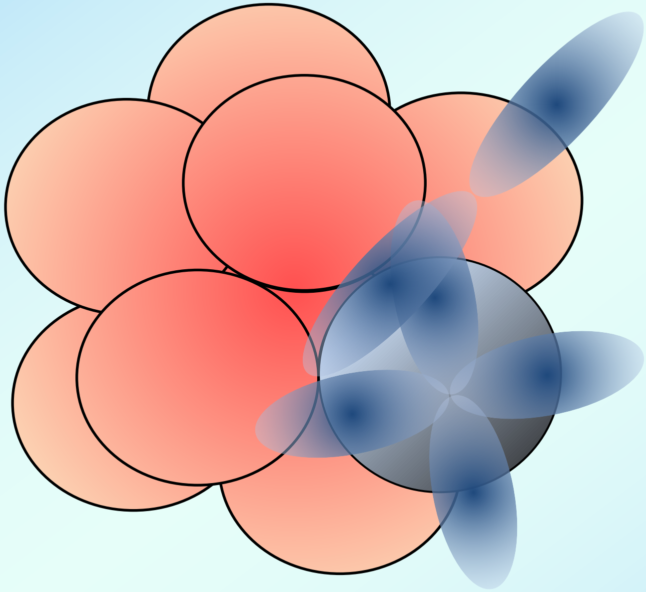

$Al_{10}Co_1$

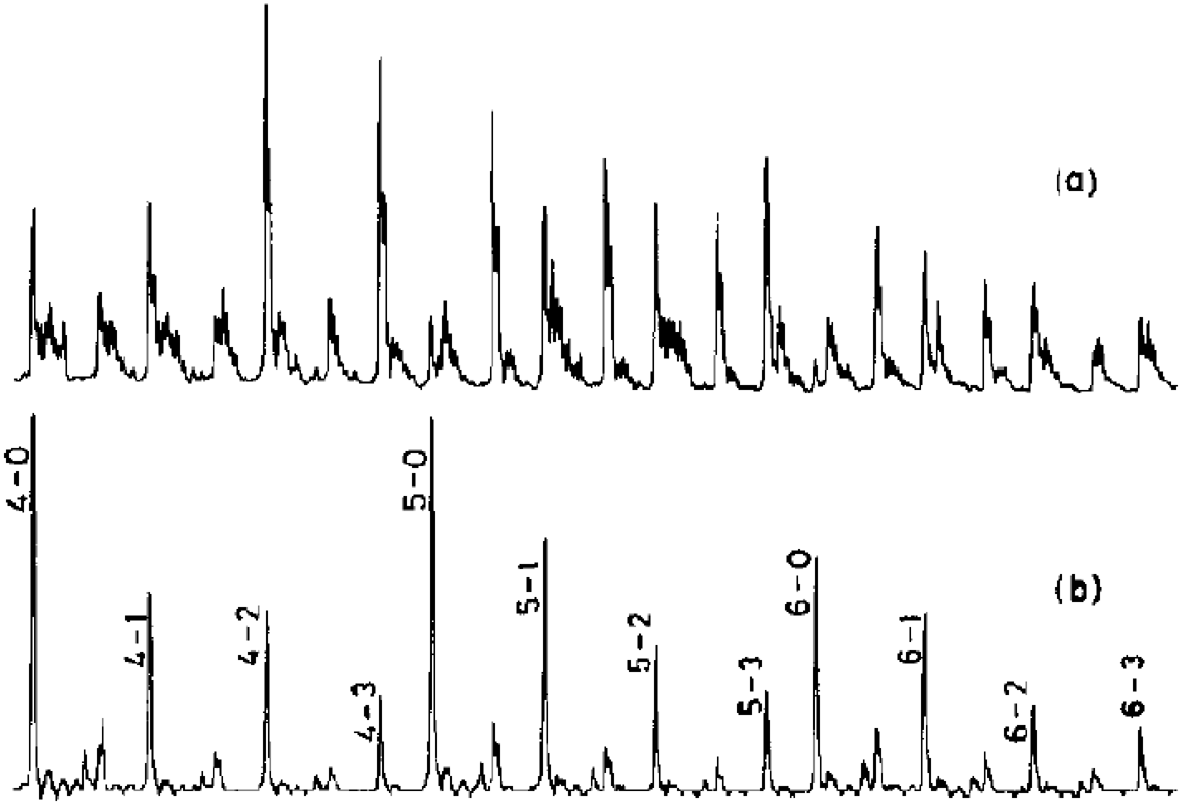

Fig. 4. TOF mass spectra of Nb_nAl_m ($n > m$) clusters (from $n=4$ to 6) reacted with (a) 100 Torr H_2 seeded in 1 atm He and (b) pure He as a reference. Peaks of the clusters are labelled according to the notation $n-m$, denoting the number of niobium atoms (n) and aluminum atoms (m), respectively.

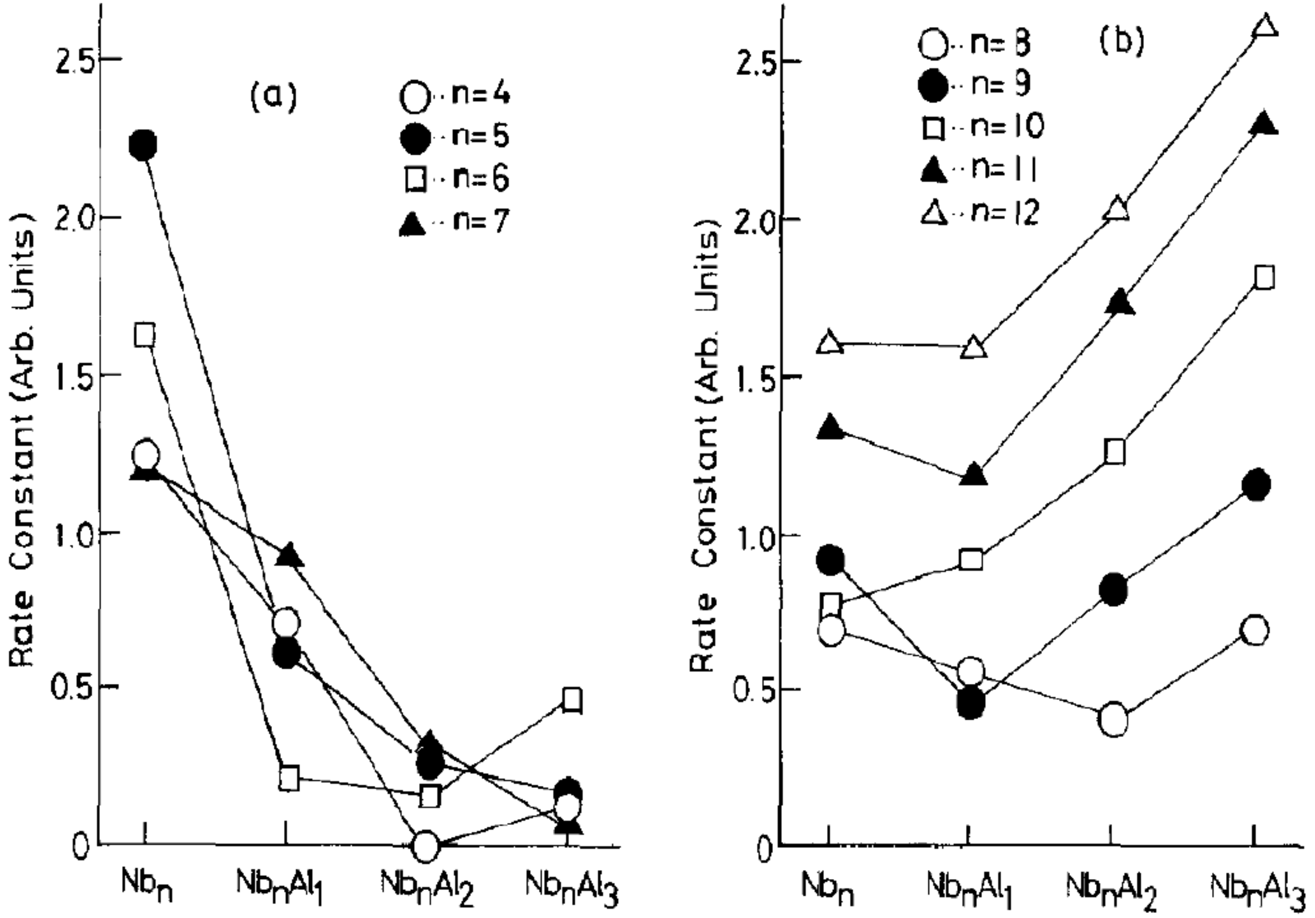

Fig. 5. The relative rate constant R_n of Nb_nAl_m ($n > m$) clusters for reaction with H_2 is plotted as a function of the number of aluminum atoms (from $m=0$ to 3). (a) Open circles, closed circles, open squares and closed triangles are R_n of Nb_4Al_m, Nb_5Al_m, Nb_6Al_m and Nb_7Al_m, respectively. (b) Open circles, closed circles, open squares, closed triangles and open triangles are R_n of Nb_8Al_m, Nb_9Al_m, $Nb_{10}Al_m$, $Nb_{11}Al_m$ and $Nb_{12}Al_m$, respectively.

茅　幸二　教授

略歴

昭和36年3月 東京大学理学部卒業
昭和56年4月 慶應義塾大学 理工学部 化学科 教授
平成11年4月 岡崎国立共同研究機構 分子科学研究所長
平成16年4月 独立行政法人理化学研究所　和光研究所長　兼　中央研究所長
平成20年4月 独立行政法人理化学研究所
　次世代スーパーコンピュータ開発実施本部　副本部長

受賞歴

平成2年3月　日本化学会学術賞（「準安定分子小集団の物性と反応」に対して）
平成13年３月日本化学会賞（「クラスター化学の創製－二成分複合効果の解明－」に対して）
平成17年11月　文化功労者顕彰

茅幸二先生から学んだこと

- 絶えず新しい独創的な研究に挑戦し続ける。
  現在の既存の研究がまずまず順調であっても固執せず、時には思いきって捨て去る。
  独自の新しい実験装置を自作する。

- 視野、見識が広い。
  相手の立場・研究分野を考慮しながら対応ができる。
  学術講演だけでなく、学生との対話においても。
  専門分野だけでなく、有機化学・物理学・生物学等の周辺分野においても。
  基礎研究だけでなく、応用研究、企業での製品開発においても。
  研究者だけでなく、霞ヶ関の官僚に対しても。
  → 研究者・教育者としてだけでなく、政治家としても超一流。
  （※先生がどんなに偉くなっても、わたしにとっては心の師匠であることに変わりはない。）

- 学生の自主性を“適度”に尊重する。
  大まかな、漠然とした指導。詳細は本人に任せる。
  （※一見、丸投げ？に見えるが・・実は全く異なる。）
  相手に応じた指導。相手の長所を存分に引き出す。

→ 卒業後、数十年が経過してもなお、多くの卒業生は先生を慕って同窓会に毎回出席する。

わたしは今や、当時の茅先生と同年代となった。
当時の茅研究室は、わたしにとって研究室の理想である。
しかし・・先生には未だに遠く及ばない。

問1.
固体の遷移金属表面にH_2が解離吸着する機構について、簡単に説明しなさい。

問2.
Fe_nクラスターとH_2との反応おいては、クラスターの構成原子数nに依存して反応速度が大きく変化する。その原因としてどのようなことが考えられるのか。大空に想像の翼を広げて、あなた自身の考えを簡単に記しなさい。

♣ クラスターの衝突反応

- ♠ Low energy cluster ion-atom collision: Collisional energy transfer and complex formation of Ar_n^+ with ^{36}Ar

Masahiko Ichihashi, Shinji Nonose, Takashi Nagata and Tamotsu Kondow
J. Chem. Phys. 100, 6458 (1994)

Experimental apparatus, Mass sepctra

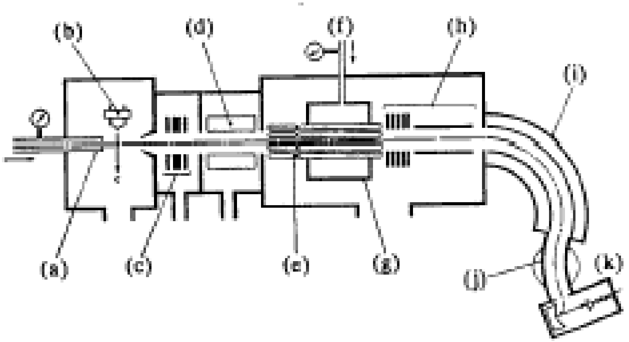

FIG. 1. Schematic drawing of the experimental apparatus. (a) Nozzle; (b) electron gun; (c) ion lens; (d) quadrupole mass filter; (e) octopole ion beam guide; (f) target gas inlet; (g) collision cell; (h) acceleration lens; (i) electrostatic sector; (j) magnetic sector; (k) detector.

$$\sigma_r = \frac{k_B T}{P l} \ln \frac{I_{\text{off}}}{I_{\text{on}}} , \qquad (2)$$

$$\sigma_p = \sigma_r \frac{I_p}{\Sigma I_p} , \qquad (3)$$

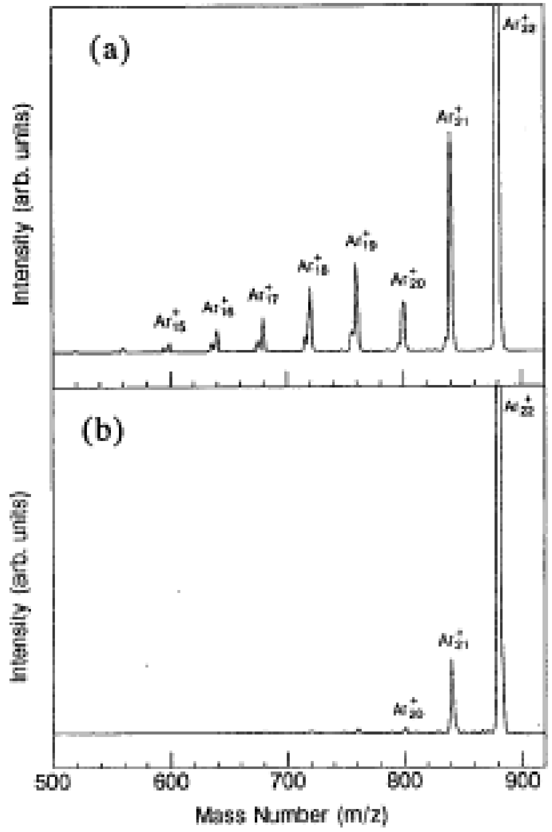

FIG. 2. Mass spectrum of the ions produced from Ar_{22}^+ in collision with ^{36}Ar (a); the ^{36}Ar pressure in the collision cell is 5.0×10^{-5} Torr. The mass spectrum of the product ions without the target gas in the collision cell is also shown in (b) for comparison.

Survival fractions, Internal temperatures, Reaction cross sections

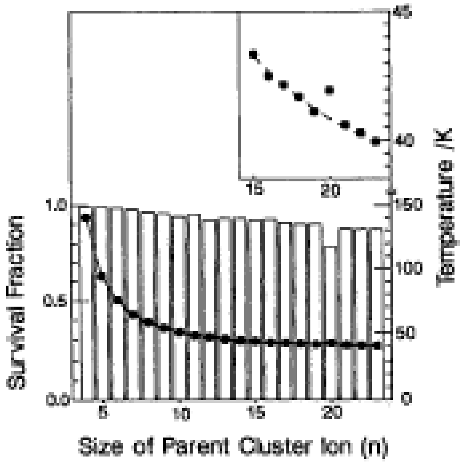

FIG. 3. Survival fractions of the parent cluster ions Ar_n^+ (histogram) and their internal temperatures (●) estimated from RRK theory. The inset shows the magnified temperature vs cluster size curve in a vicinity of $n=20$; the deviation of the temperature at $n=20$ is related to the stability of Ar_{20}^+ (see the text).

$$k_n = A\left(\frac{E_0 - V_n}{E_0}\right)^{3n-7}, \tag{5}$$

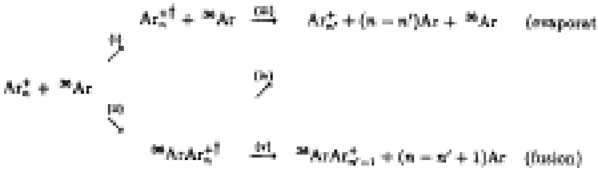

$$\begin{tikzcd}
 & Ar_n^{+\dagger} + {}^{36}Ar \arrow[r, "(iii)"] & Ar_{n'}^+ + (n-n')Ar + {}^{36}Ar \quad \text{(evaporation)} \quad (7) \\
Ar_n^+ + {}^{36}Ar \arrow[ur, "(i)"] \arrow[dr, "(ii)"'] & & \\
 & {}^{36}ArAr_n^{+\dagger} \arrow[uu, phantom] \arrow[uur, "(iv)"] \arrow[r, "(v)"] & {}^{36}ArAr_{n'-1}^+ + (n-n'+1)Ar \quad \text{(fusion)} \quad (8)
\end{tikzcd}$$

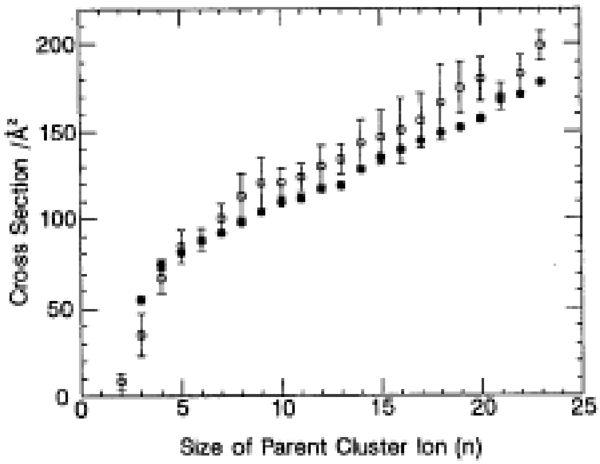

FIG. 4. Reaction cross sections (○) are plotted against the size n of the parent cluster ion Ar_n^+. The calculated cross sections (●) are shown as a comparison. The collision energy is 0.2 eV in the center-of-mass frame.

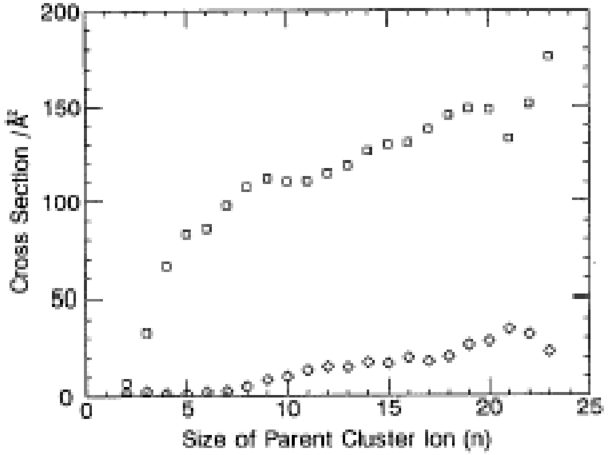

FIG. 5. Evaporation (□) and fusion (◇) cross sections are plotted against the size n of the parent cluster ion Ar_n^+ at the collision energy of 0.2 eV in the center-of-mass frame.

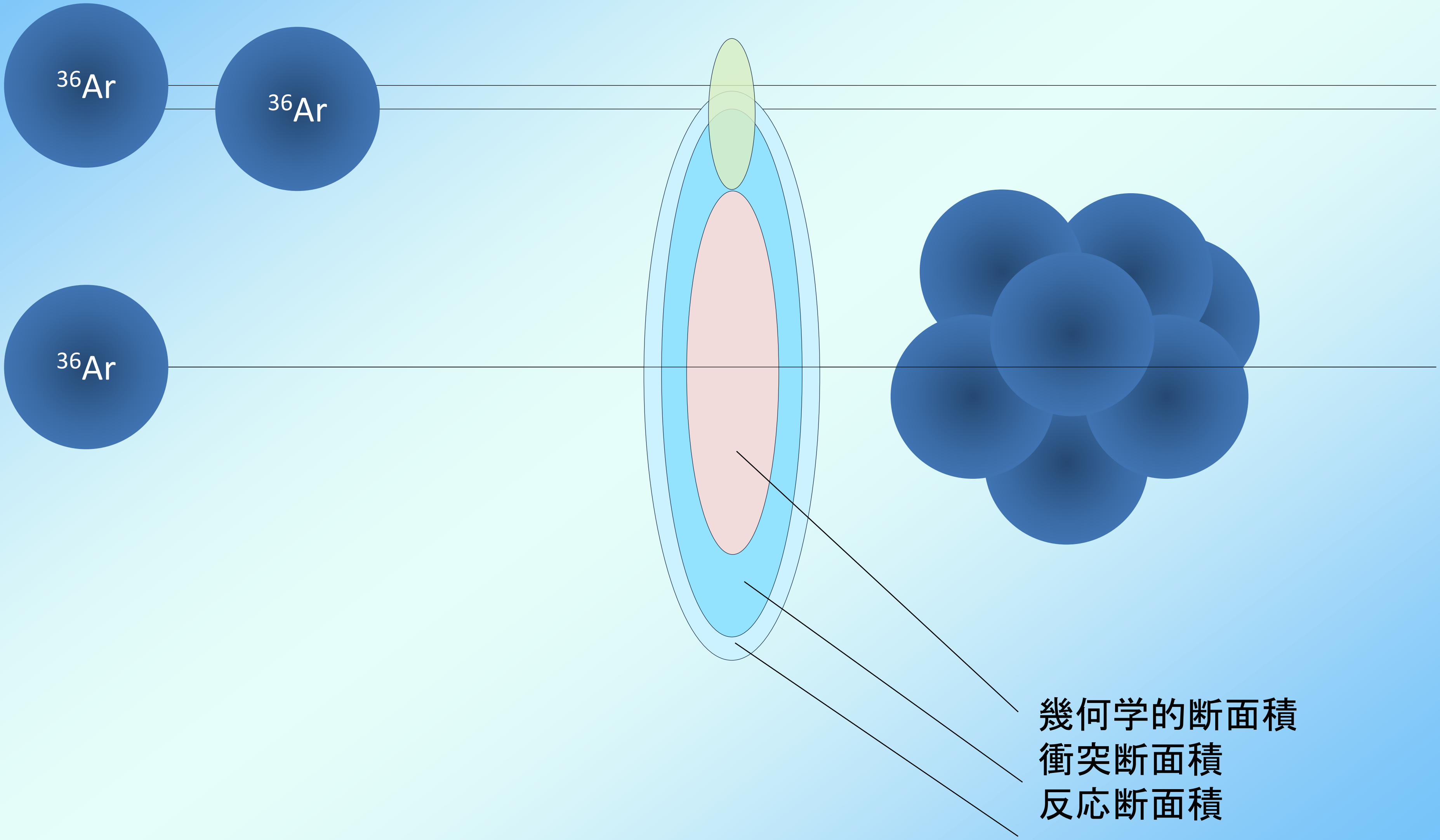

幾何学的断面積
衝突断面積
反応断面積

Evaporative Ensemble Model

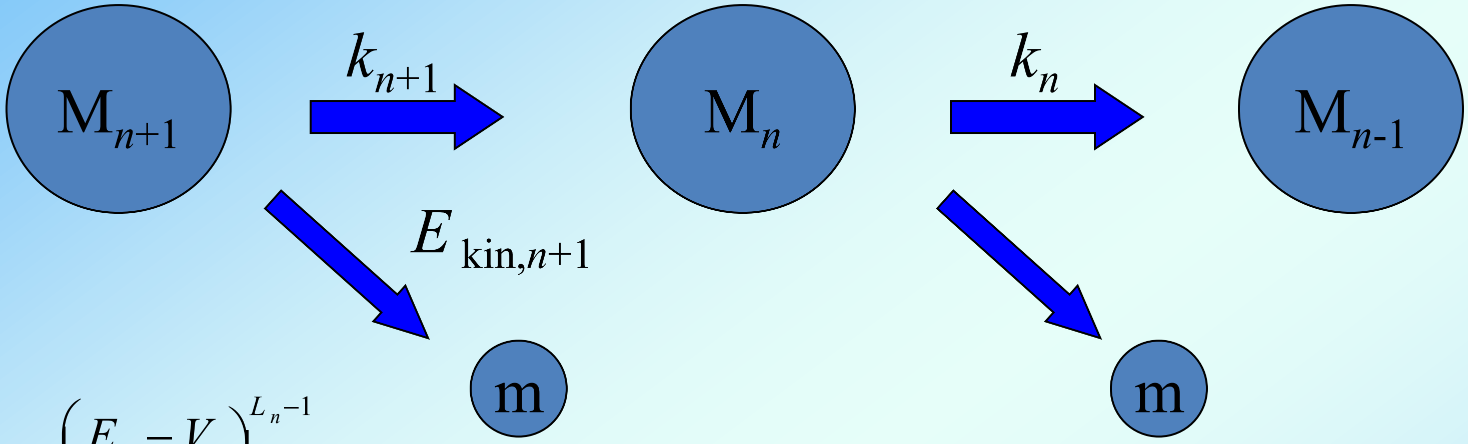

M_{n+1} $\xrightarrow{k_{n+1}}$ M_n $\xrightarrow{k_n}$ $\mathrm{M}_{n\text{-}1}$

$E_{\mathrm{kin},n+1}$

m

m

$$k_n = A\left(\frac{E_n - V_n}{E_n}\right)^{L_n - 1}$$

$$k_{n+1} = A\left(\frac{E_{n+1} - V_{n+1}}{E_{n+1}}\right)^{L_{n+1} - 1}$$

$$E_n = E_{n+1} - V_{n+1} - E_{kin,n+1}$$

$$E_{kin,n+1} = 2\left(\frac{E_{n+1} - V_{n+1}}{L_{n+1} - 1}\right)$$

$$P_n = \left(\frac{k_{n+1}}{k_{n+1} - k_n}\right)\left[\exp(-k_n t_1) - \exp(-k_{n+1} t_1)\right]$$

$$P_{n-1} = P_n\left[1 - \exp(-k_n t_2)\right]$$

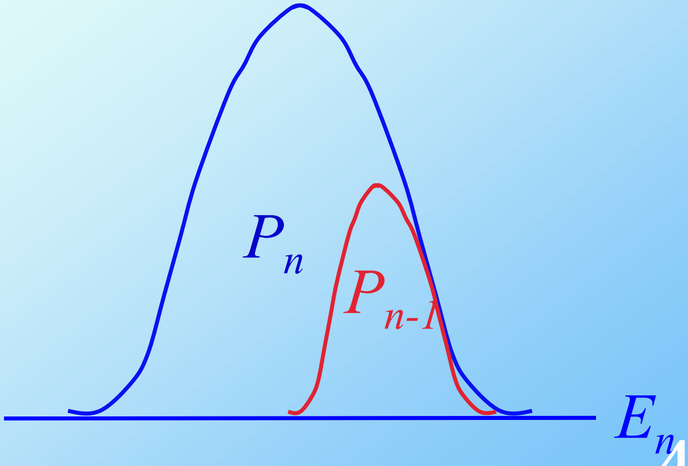

Branching fractions of product ions

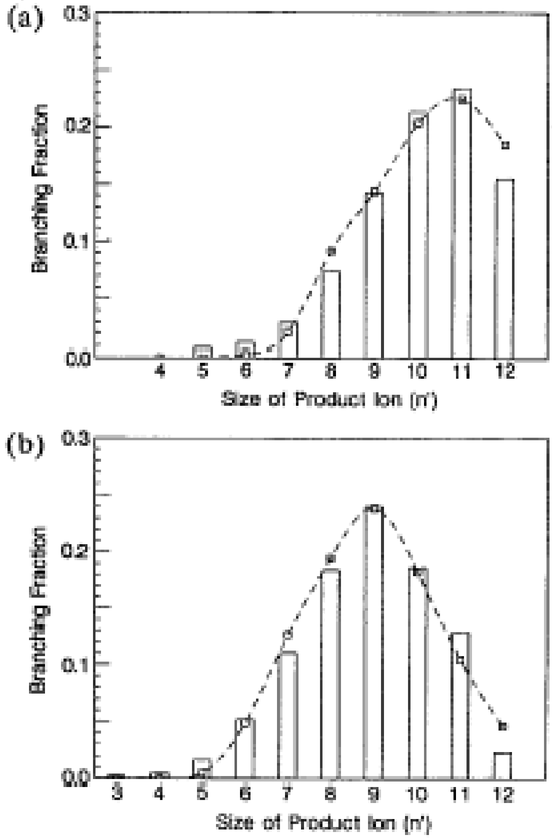

FIG. 6. Branching fractions of the product ions for the evaporation in the collision of Ar_{13}^+ with ^{36}Ar at the center-of-mass collision energies of (a) 0.2 and (b) 2.0 eV. The plots indicated by the symbol ☐ show the branching fractions calculated from RRK theory.

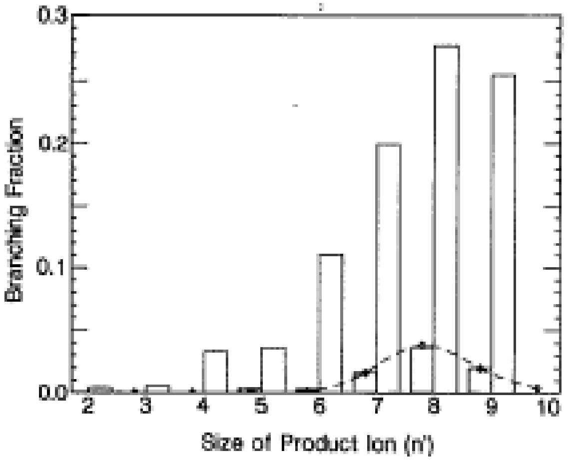

FIG. 7. Branching fractions of the product ions for the evaporation [$Ar_{n'}^+$, (open histogram) and fusion [$^{36}ArAr_{n'-1}^+$ (shaded histogram)] in the collision of Ar_{10}^+ with ^{36}Ar at the collision energy of 0.2 eV in the center-of-mass frame. The symbols ◇ show the branching fractions calculated from RRK theory.

♠ Role of electron pairing in collisional dissociation of Na_9^+ by a rare-gas atom

Shinji Nonose, Hideki Tanaka, Tomoyuki Mizuno, Jun Hirokawa and Tamotsu Kondow
J. Chem. Phys. 104, 5869 (1996)

Experimental, Results

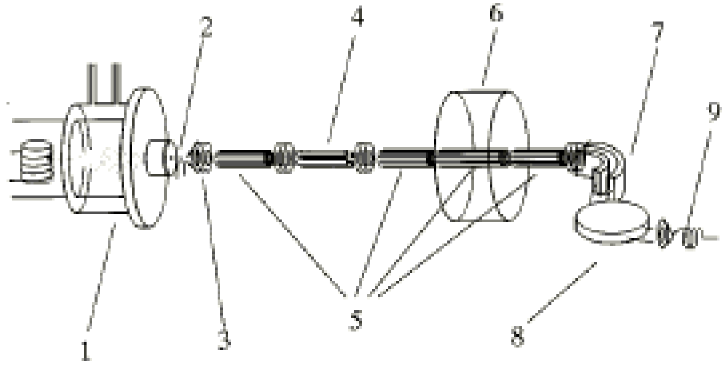

FIG. 1. Schematic diagram of the experimental apparatus: (1) cluster source, (2) electron gun, (3) skimmer lens, (4) quadrupole mass filter, (5) octopole ion beam guides, (6) collision cell, (7) electrostatic sector, (8) magnetic sector, and (9) detector.

$$Na_9^+ \xrightarrow{RG} Na_8^+ + Na, \tag{6}$$

$$Na_9^+ \xrightarrow{RG} Na_7^+ + Na_2\,. \tag{7}$$

$$Na_9^+ \xrightarrow{RG} [\, Na_9^+]^\dagger, \tag{8}$$

$$[\, Na_9^+]^\dagger \rightarrow Na_7^+ + Na_2\,, \tag{9}$$

$$[\, Na_9^+]^\dagger \rightarrow Na_8^+ + Na. \tag{10}$$

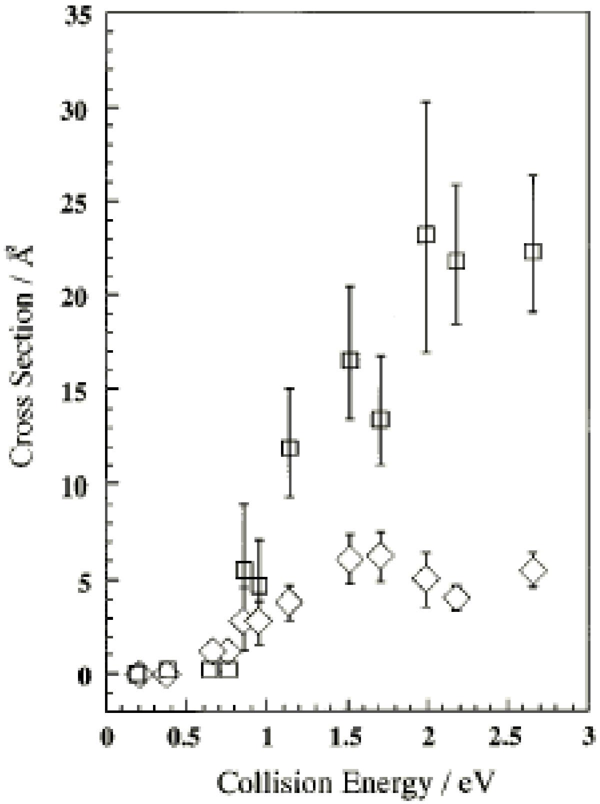

FIG. 2. Collision-energy dependence of the cross sections for the Na_2 (□) and the Na (◇) release from Na_9^+ in the collision of He.

Correlation diagrams of Na release

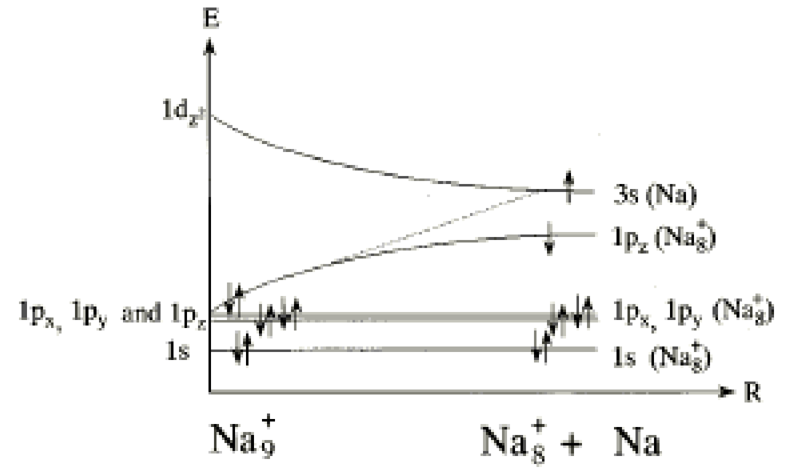

FIG. 3. Correlation diagram for the Na release from Na_9^+ along the distance between Na and Na_8^+. The left hand side of the diagram corresponds to the energies of orbitals of Na_9^+ related to the Na release, while the right hand side does to those of Na + Na_8^+.

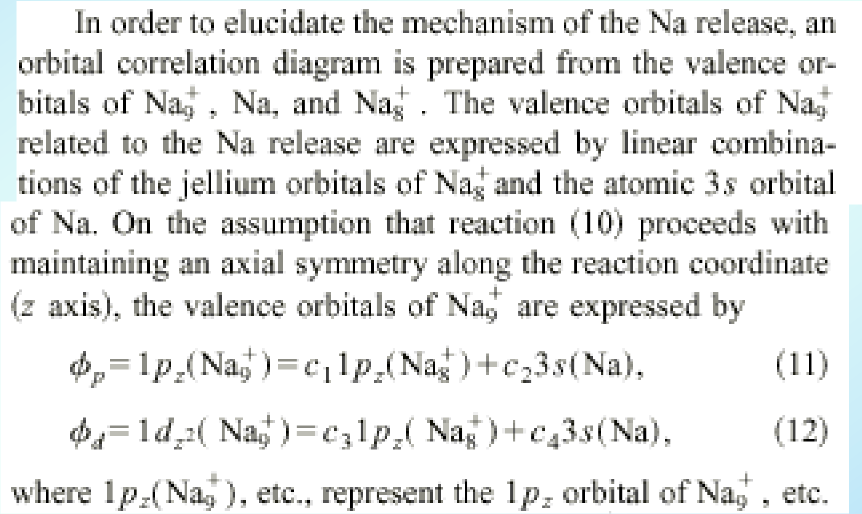

In order to elucidate the mechanism of the Na release, an orbital correlation diagram is prepared from the valence orbitals of Na_9^+, Na, and Na_8^+. The valence orbitals of Na_9^+ related to the Na release are expressed by linear combinations of the jellium orbitals of Na_8^+ and the atomic $3s$ orbital of Na. On the assumption that reaction (10) proceeds with maintaining an axial symmetry along the reaction coordinate (z axis), the valence orbitals of Na_9^+ are expressed by

$$\phi_p = 1p_z(\mathrm{Na}_9^+) = c_1 1p_z(\mathrm{Na}_8^+) + c_2 3s(\mathrm{Na}), \qquad (11)$$

$$\phi_d = 1d_{z^2}(\mathrm{Na}_9^+) = c_3 1p_z(\mathrm{Na}_8^+) + c_4 3s(\mathrm{Na}), \qquad (12)$$

where $1p_z(\mathrm{Na}_9^+)$, etc., represent the $1p_z$ orbital of Na_9^+, etc.

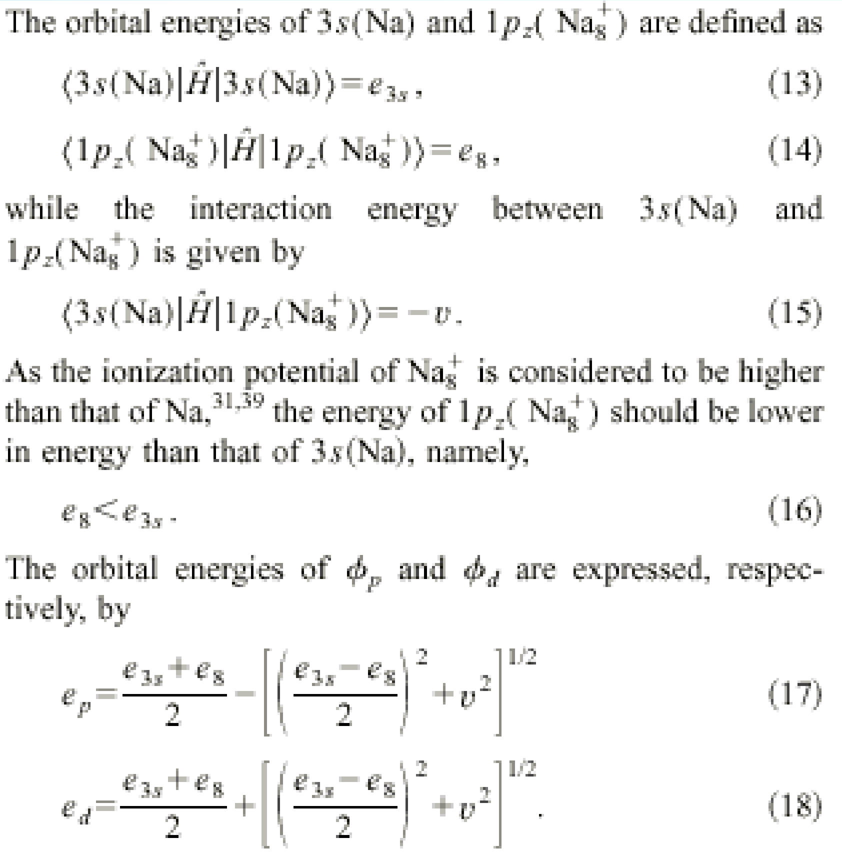

The orbital energies of $3s$(Na) and $1p_z$(Na_8^+) are defined as

$$\langle 3s(\mathrm{Na})|\hat{H}|3s(\mathrm{Na})\rangle = e_{3s}, \qquad (13)$$

$$\langle 1p_z(\mathrm{Na}_8^+)|\hat{H}|1p_z(\mathrm{Na}_8^+)\rangle = e_8, \qquad (14)$$

while the interaction energy between $3s$(Na) and $1p_z$(Na_8^+) is given by

$$\langle 3s(\mathrm{Na})|\hat{H}|1p_z(\mathrm{Na}_8^+)\rangle = -v. \qquad (15)$$

As the ionization potential of Na_8^+ is considered to be higher than that of Na,[31,39] the energy of $1p_z$(Na_8^+) should be lower in energy than that of $3s$(Na), namely,

$$e_8 < e_{3s}. \qquad (16)$$

The orbital energies of ϕ_p and ϕ_d are expressed, respectively, by

$$e_p = \frac{e_{3s}+e_8}{2} - \left[\left(\frac{e_{3s}-e_8}{2}\right)^2 + v^2\right]^{1/2} \qquad (17)$$

$$e_d = \frac{e_{3s}+e_8}{2} + \left[\left(\frac{e_{3s}-e_8}{2}\right)^2 + v^2\right]^{1/2}. \qquad (18)$$

Potential energy curve along reaction coordinate of Na_9^+ - Na_8^+ + Na

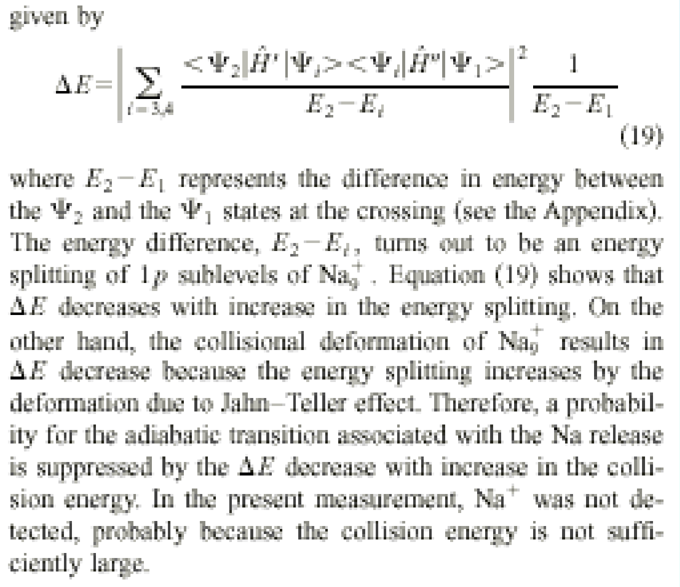

The energy gap at the crossing, ΔE, shown in Fig. 4, is given by

$$\Delta E=\left|\sum_{i=3,4}\frac{<\Psi_2|\hat{H}'|\Psi_i><\Psi_i|\hat{H}''|\Psi_1>}{E_2-E_i}\right|^2\frac{1}{E_2-E_1} \tag{19}$$

where E_2-E_1 represents the difference in energy between the Ψ_2 and the Ψ_1 states at the crossing (see the Appendix). The energy difference, E_2-E_i, turns out to be an energy splitting of $1p$ sublevels of Na_9^+. Equation (19) shows that ΔE decreases with increase in the energy splitting. On the other hand, the collisional deformation of Na_9^+ results in ΔE decrease because the energy splitting increases by the deformation due to Jahn–Teller effect. Therefore, a probability for the adiabatic transition associated with the Na release is suppressed by the ΔE decrease with increase in the collision energy. In the present measurement, Na^+ was not detected, probably because the collision energy is not sufficiently large.

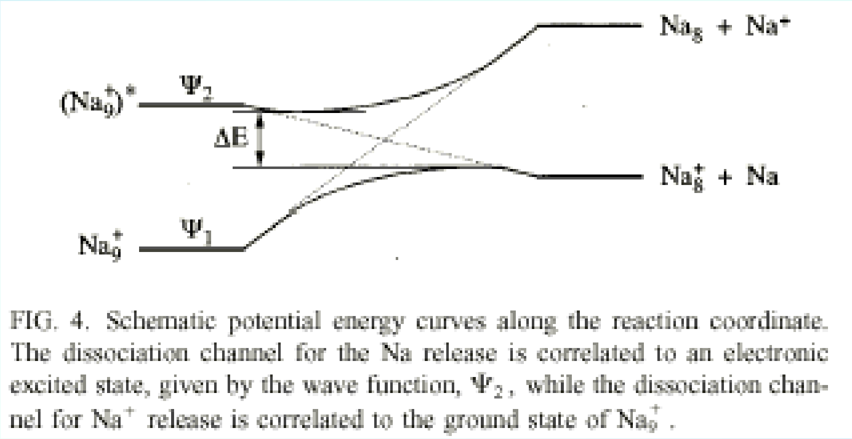

FIG. 4. Schematic potential energy curves along the reaction coordinate. The dissociation channel for the Na release is correlated to an electronic excited state, given by the wave function, Ψ_2, while the dissociation channel for Na^+ release is correlated to the ground state of Na_9^+.

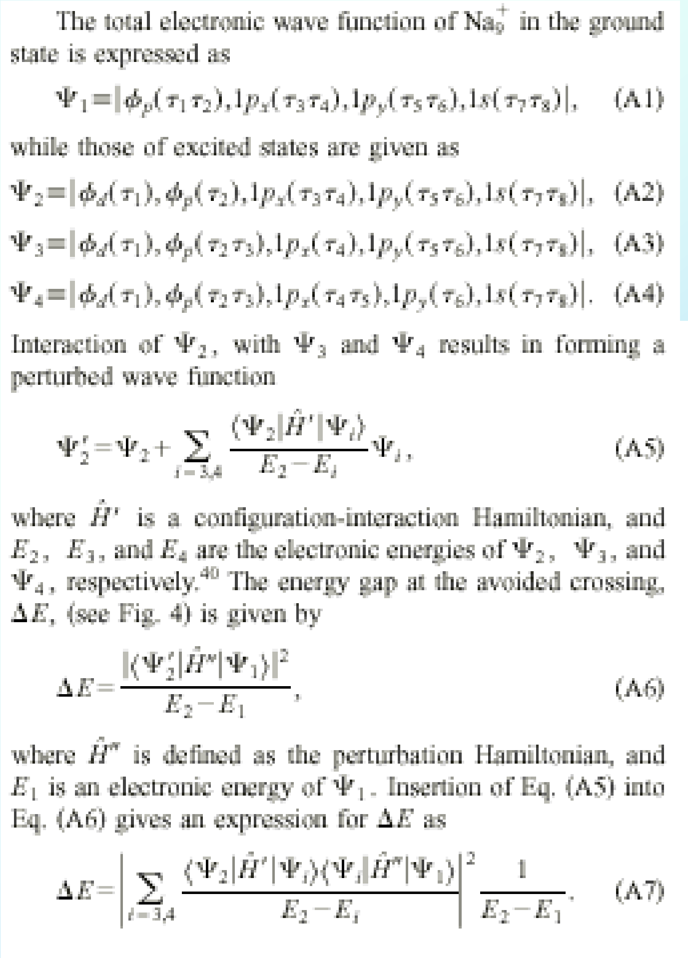

The total electronic wave function of Na_9^+ in the ground state is expressed as

$$\Psi_1=|\phi_p(\tau_1\tau_2),1p_x(\tau_3\tau_4),1p_y(\tau_5\tau_6),1s(\tau_7\tau_8)|, \tag{A1}$$

while those of excited states are given as

$$\Psi_2=|\phi_d(\tau_1),\phi_p(\tau_2),1p_x(\tau_3\tau_4),1p_y(\tau_5\tau_6),1s(\tau_7\tau_8)|, \tag{A2}$$

$$\Psi_3=|\phi_d(\tau_1),\phi_p(\tau_2\tau_3),1p_x(\tau_4),1p_y(\tau_5\tau_6),1s(\tau_7\tau_8)|, \tag{A3}$$

$$\Psi_4=|\phi_d(\tau_1),\phi_p(\tau_2\tau_3),1p_x(\tau_4\tau_5),1p_y(\tau_6),1s(\tau_7\tau_8)|. \tag{A4}$$

Interaction of Ψ_2, with Ψ_3 and Ψ_4 results in forming a perturbed wave function

$$\Psi_2'=\Psi_2+\sum_{i=3,4}\frac{\langle\Psi_2|\hat{H}'|\Psi_i\rangle}{E_2-E_i}\Psi_i, \tag{A5}$$

where $\hat{H}'$ is a configuration-interaction Hamiltonian, and E_2, E_3, and E_4 are the electronic energies of Ψ_2, Ψ_3, and Ψ_4, respectively.[40] The energy gap at the avoided crossing, ΔE, (see Fig. 4) is given by

$$\Delta E=\frac{|\langle\Psi_2'|\hat{H}''|\Psi_1\rangle|^2}{E_2-E_1}, \tag{A6}$$

where $\hat{H}''$ is defined as the perturbation Hamiltonian, and E_1 is an electronic energy of Ψ_1. Insertion of Eq. (A5) into Eq. (A6) gives an expression for ΔE as

$$\Delta E=\left|\sum_{i=3,4}\frac{\langle\Psi_2|\hat{H}'|\Psi_i\rangle\langle\Psi_i|\hat{H}''|\Psi_1\rangle}{E_2-E_i}\right|^2\frac{1}{E_2-E_1}. \tag{A7}$$

Correlation diagrams of Na_2 release

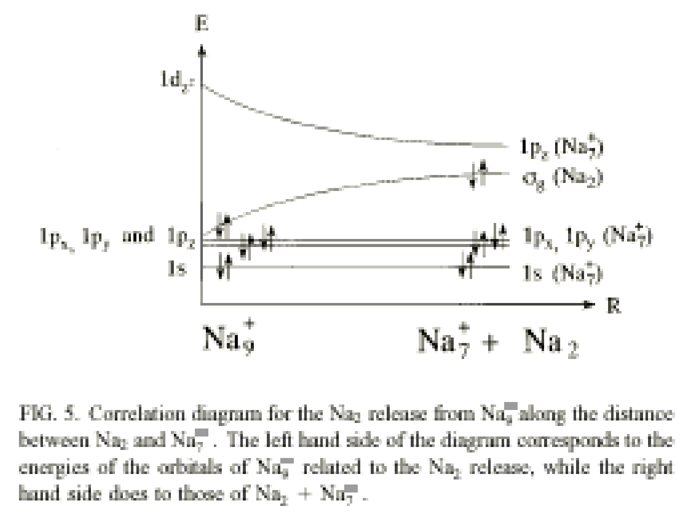

FIG. 5. Correlation diagram for the Na_2 release from Na_9^+ along the distance between Na_2 and Na_7^+. The left hand side of the diagram corresponds to the energies of the orbitals of Na_9^+ related to the Na_2 release, while the right hand side does to those of $Na_2 + Na_7^+$.

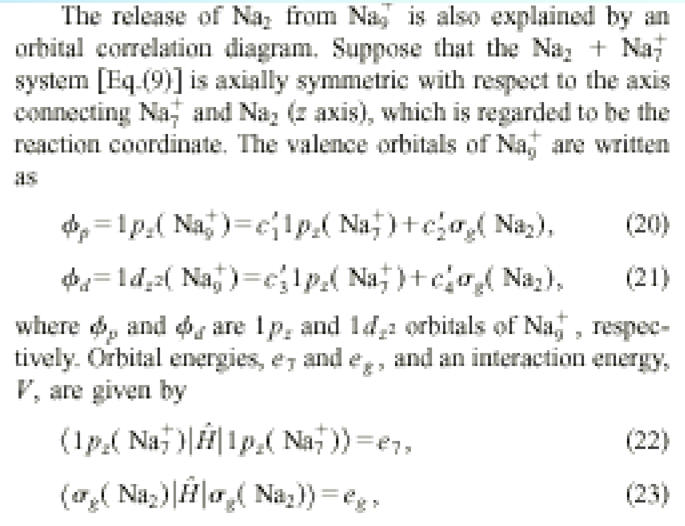

The release of Na_2 from Na_9^+ is also explained by an orbital correlation diagram. Suppose that the $Na_2 + Na_7^+$ system [Eq.(9)] is axially symmetric with respect to the axis connecting Na_7^+ and Na_2 (z axis), which is regarded to be the reaction coordinate. The valence orbitals of Na_9^+ are written as

$$\phi_p = 1p_z(\mathrm{Na}_9^+) = c_1' 1p_z(\mathrm{Na}_7^+) + c_2' \sigma_g(\mathrm{Na}_2), \tag{20}$$

$$\phi_d = 1d_{z^2}(\mathrm{Na}_9^+) = c_3' 1p_z(\mathrm{Na}_7^+) + c_4' \sigma_g(\mathrm{Na}_2), \tag{21}$$

where ϕ_p and ϕ_d are $1p_z$ and $1d_{z^2}$ orbitals of Na_9^+, respectively. Orbital energies, e_7 and e_g, and an interaction energy, V, are given by

$$\langle 1p_z(\mathrm{Na}_7^+)|\hat{H}|1p_z(\mathrm{Na}_7^+)\rangle = e_7, \tag{22}$$

$$\langle \sigma_g(\mathrm{Na}_2)|\hat{H}|\sigma_g(\mathrm{Na}_2)\rangle = e_g, \tag{23}$$

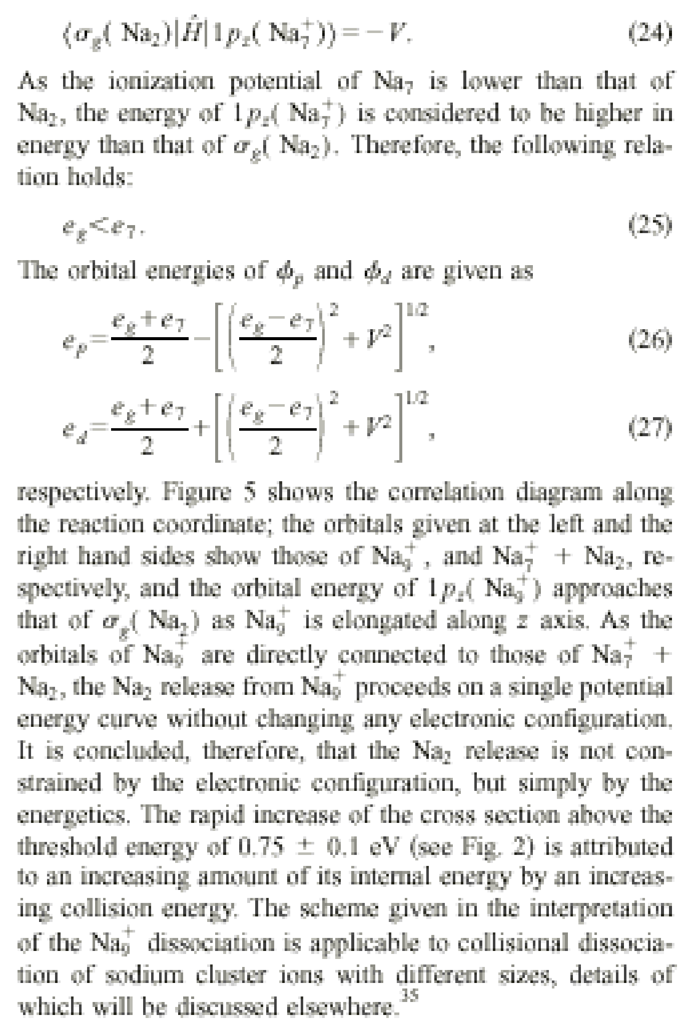

$$\langle \sigma_g(\mathrm{Na}_2)|\hat{H}|1p_z(\mathrm{Na}_7^+)\rangle = -V. \tag{24}$$

As the ionization potential of Na_7 is lower than that of Na_2, the energy of $1p_z(Na_7^+)$ is considered to be higher in energy than that of $\sigma_g(Na_2)$. Therefore, the following relation holds:

$$e_g < e_7. \tag{25}$$

The orbital energies of ϕ_p and ϕ_d are given as

$$e_p = \frac{e_g + e_7}{2} - \left[\left(\frac{e_g - e_7}{2}\right)^2 + V^2\right]^{1/2}, \tag{26}$$

$$e_d = \frac{e_g + e_7}{2} + \left[\left(\frac{e_g - e_7}{2}\right)^2 + V^2\right]^{1/2}, \tag{27}$$

respectively. Figure 5 shows the correlation diagram along the reaction coordinate; the orbitals given at the left and the right hand sides show those of Na_9^+, and $Na_7^+ + Na_2$, respectively, and the orbital energy of $1p_z(Na_9^+)$ approaches that of $\sigma_g(Na_2)$ as Na_9^+ is elongated along z axis. As the orbitals of Na_9^+ are directly connected to those of $Na_7^+ + Na_2$, the Na_2 release from Na_9^+ proceeds on a single potential energy curve without changing any electronic configuration. It is concluded, therefore, that the Na_2 release is not constrained by the electronic configuration, but simply by the energetics. The rapid increase of the cross section above the threshold energy of 0.75 ± 0.1 eV (see Fig. 2) is attributed to an increasing amount of its internal energy by an increasing collision energy. The scheme given in the interpretation of the Na_9^+ dissociation is applicable to collisional dissociation of sodium cluster ions with different sizes, details of which will be discussed elsewhere.[35]

共同研究者

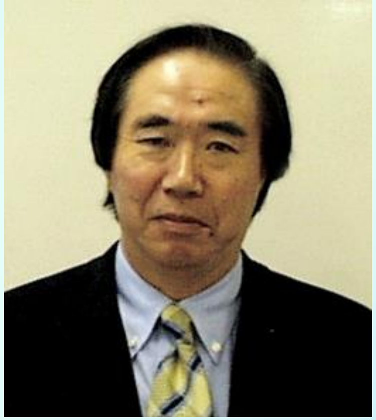

近藤保　東京大学名誉教授
豊田工業大学　クラスター研究室　創設者

永田 敬　総合研究大学院大学 理事・副学長

廣川淳　北海道大学大学院地球環境科学分野准教授

市橋正彦　豊田工業大学教授

田中秀樹　中央大学応用化学科教授

♠ Collisional reactions of Al_n^+ with Rg

1. O. Ingolfsson, H. Takeo and S. Nonose, *J. Chem. Phys*., **110** 4382-4393 (1999).
2. O. Ingolfsson, H. Takeo and S. Nonose, *Chem. Phys. Lett.,* **311** 421-427 (1999).

Apparatus

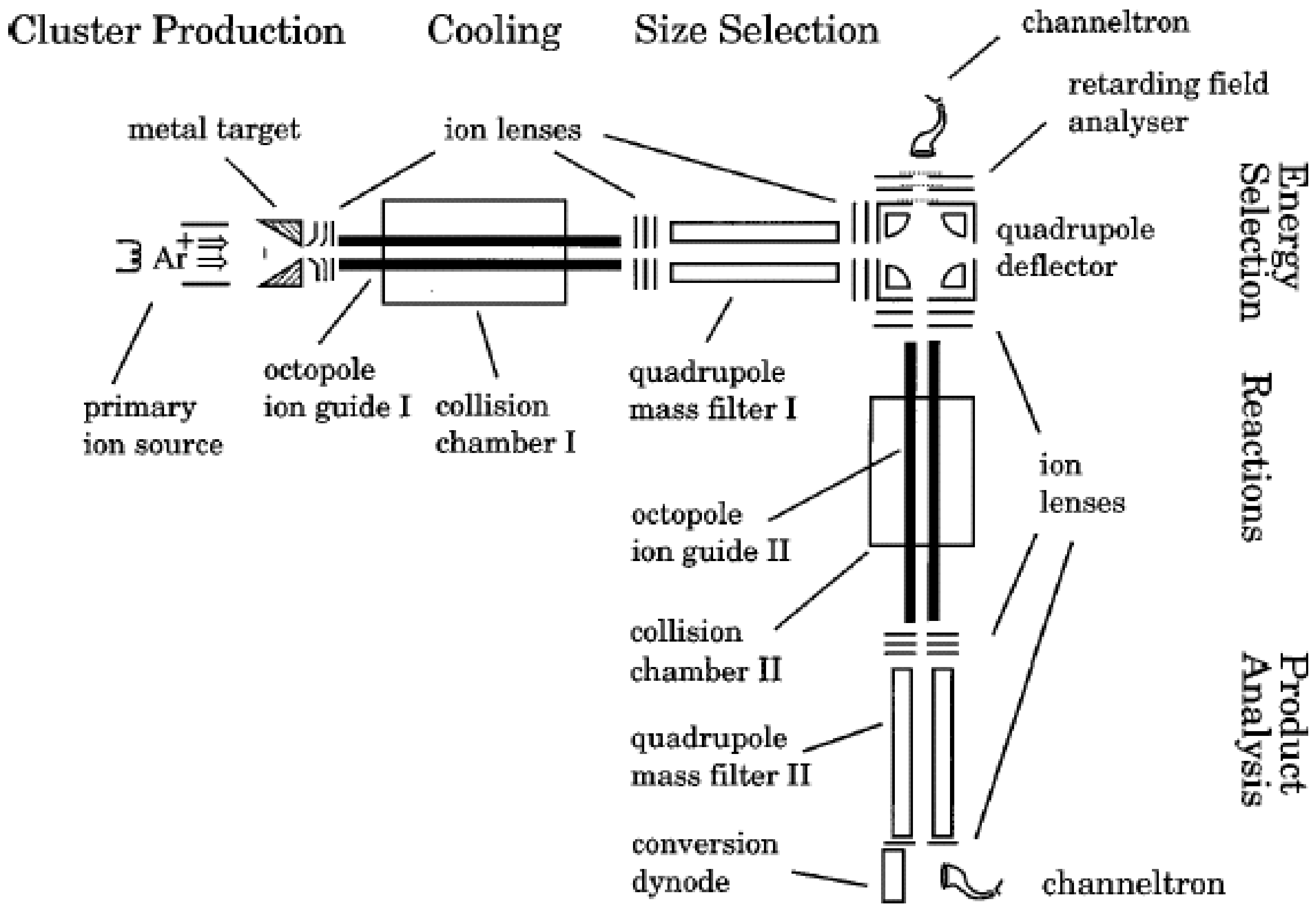

FIG. 1. Schematic of the apparatus.

Mass spectra of Al_n^+

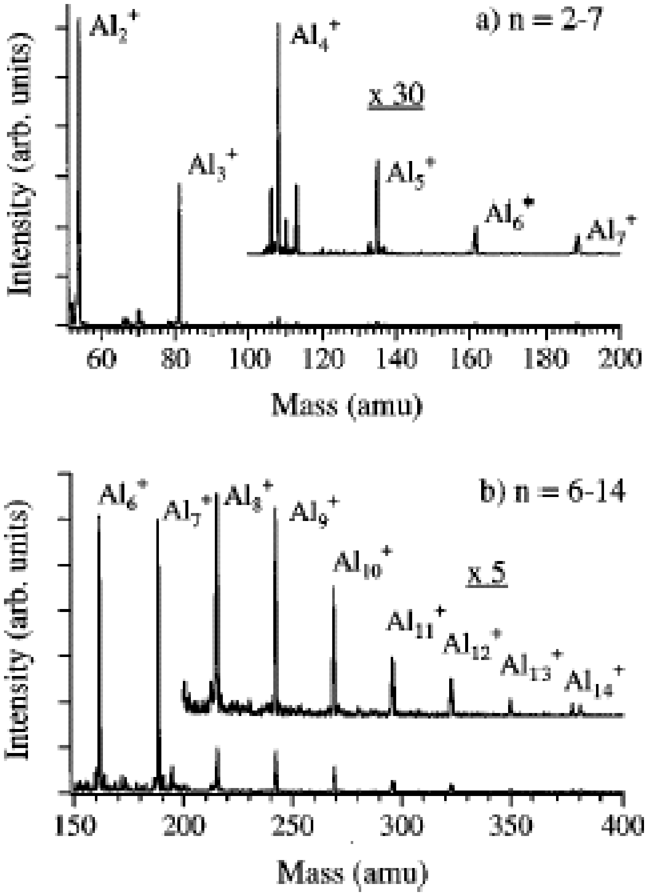

FIG. 2. Mass spectra of the stable Al_n^+ clusters, recorded by scanning the second quadrupole with the first quadrupole permitting transmission of al ions (dc off). (a) $n = 2-7$, (b) $n = 6-14$. Note the different mass range.

Energy dependence of dissociation cross sections

$$\mathrm{Al}_n^+ \rightarrow \mathrm{Al}^+ + \mathrm{Al}_{n-1},$$

$$\mathrm{Al}_n^+ \rightarrow \mathrm{Al}_{n-1}^+ + \mathrm{Al}.$$

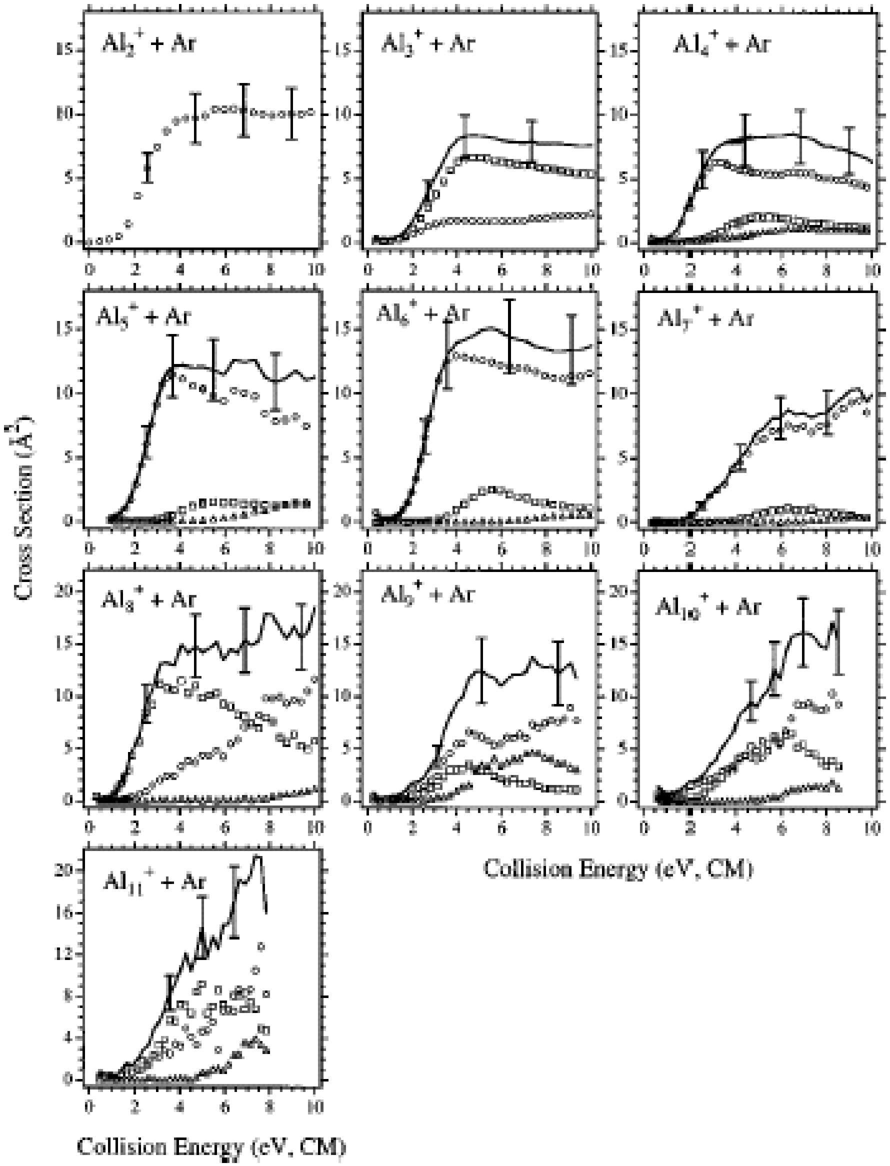

FIG. 3. Energy dependence of the total and the partial dissociation cross sections for Al_n^+ ($n=2-11$) upon collision with argon. The total CID cross section is shown as solid lines, the Al^+ release as open circles, ○, and the neutral Al atom release as open squares, □. The release of two neutral Al atoms is shown as open triangles, △. Note the different scale for $n=2-7$ and $n=8-11$.

Correlation diagrams of Al_2 +Al^+ and Al_2^+ + Al

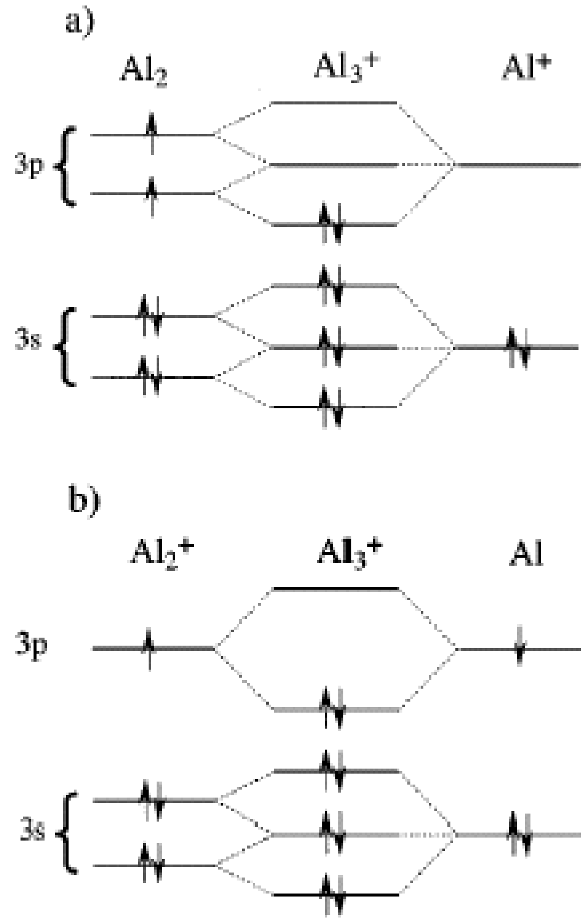

FIG. 4. Correlation diagram for (a) Al_2+Al^+ and (b) $Al_2^+ + Al$. The combination of the triplet Al_2 ground state with the singlet Al^+ to form the singlet Al_3^+ ground state, is not possible under spin conservation.

Correlation diagrams of Al release

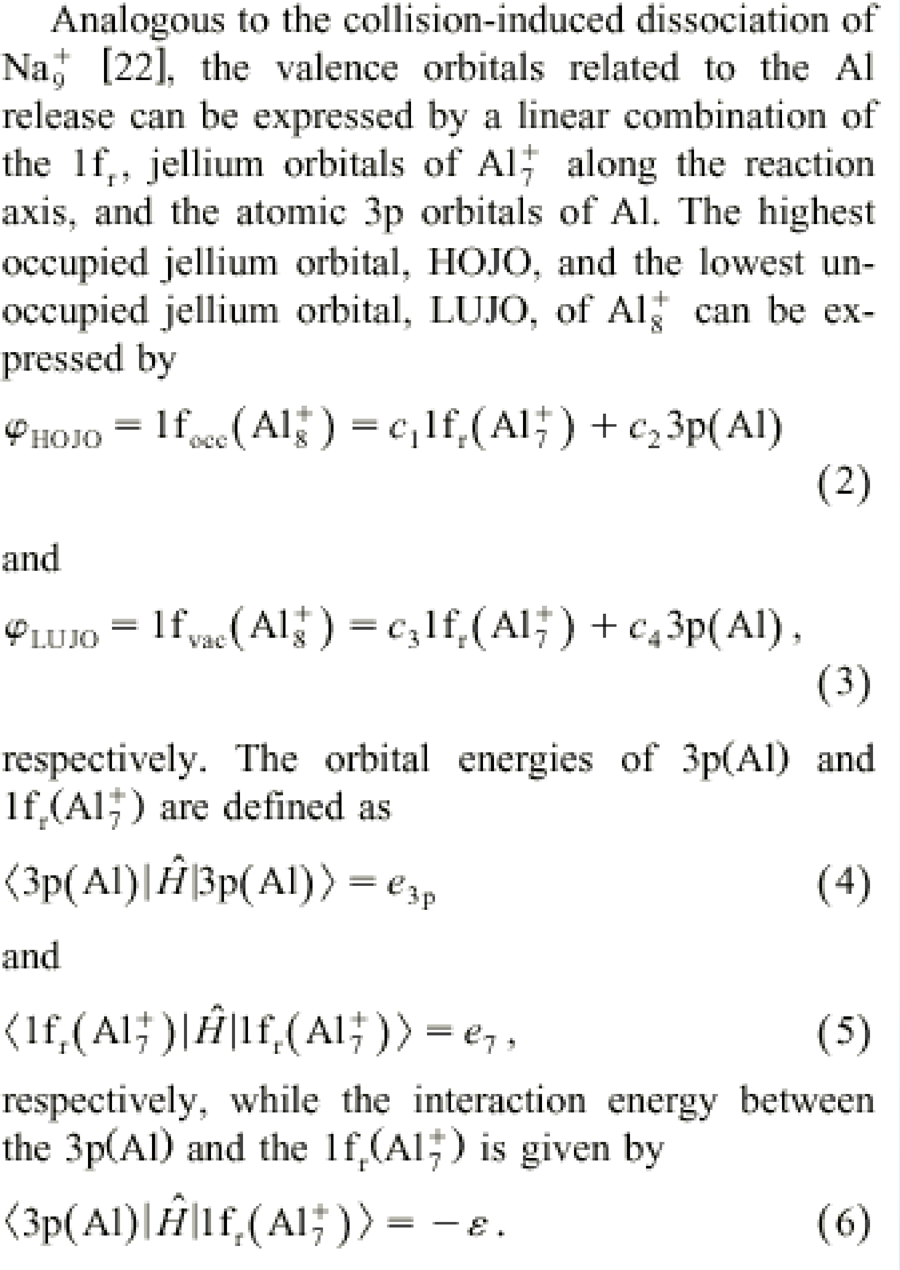

Analogous to the collision-induced dissociation of Na_9^+ [22], the valence orbitals related to the Al release can be expressed by a linear combination of the $1f_r$, jellium orbitals of Al_7^+ along the reaction axis, and the atomic 3p orbitals of Al. The highest occupied jellium orbital, HOJO, and the lowest unoccupied jellium orbital, LUJO, of Al_8^+ can be expressed by

$$\varphi_{\mathrm{HOJO}} = 1f_{\mathrm{occ}}(Al_8^+) = c_1 1f_r(Al_7^+) + c_2 3p(Al) \tag{2}$$

and

$$\varphi_{\mathrm{LUJO}} = 1f_{\mathrm{vac}}(Al_8^+) = c_3 1f_r(Al_7^+) + c_4 3p(Al)\,, \tag{3}$$

respectively. The orbital energies of 3p(Al) and $1f_r(Al_7^+)$ are defined as

$$\langle 3p(Al)|\hat{H}|3p(Al)\rangle = e_{3p} \tag{4}$$

and

$$\langle 1f_r(Al_7^+)|\hat{H}|1f_r(Al_7^+)\rangle = e_7\,, \tag{5}$$

respectively, while the interaction energy between the 3p(Al) and the $1f_r(Al_7^+)$ is given by

$$\langle 3p(Al)|\hat{H}|1f_r(Al_7^+)\rangle = -\varepsilon\,. \tag{6}$$

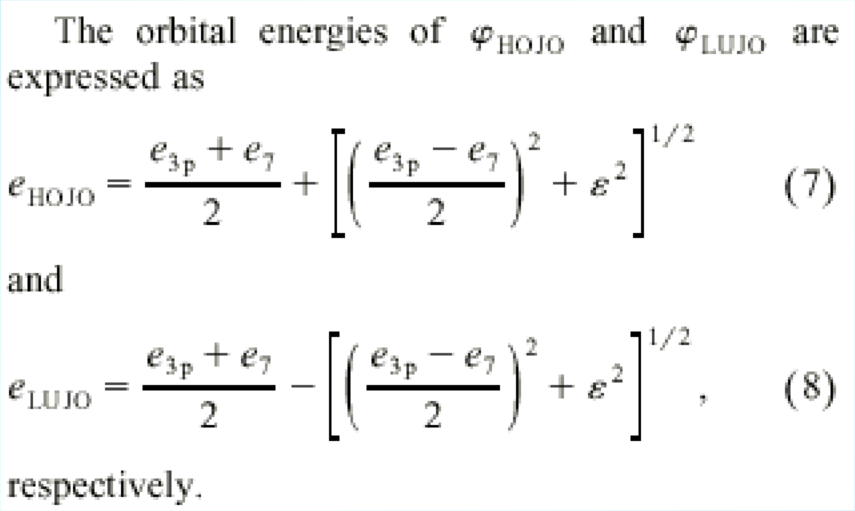

The orbital energies of φ_{HOJO} and φ_{LUJO} are expressed as

$$e_{\mathrm{HOJO}} = \frac{e_{3p} + e_7}{2} + \left[\left(\frac{e_{3p} - e_7}{2}\right)^2 + \varepsilon^2\right]^{1/2} \tag{7}$$

and

$$e_{\mathrm{LUJO}} = \frac{e_{3p} + e_7}{2} - \left[\left(\frac{e_{3p} - e_7}{2}\right)^2 + \varepsilon^2\right]^{1/2}, \tag{8}$$

respectively.

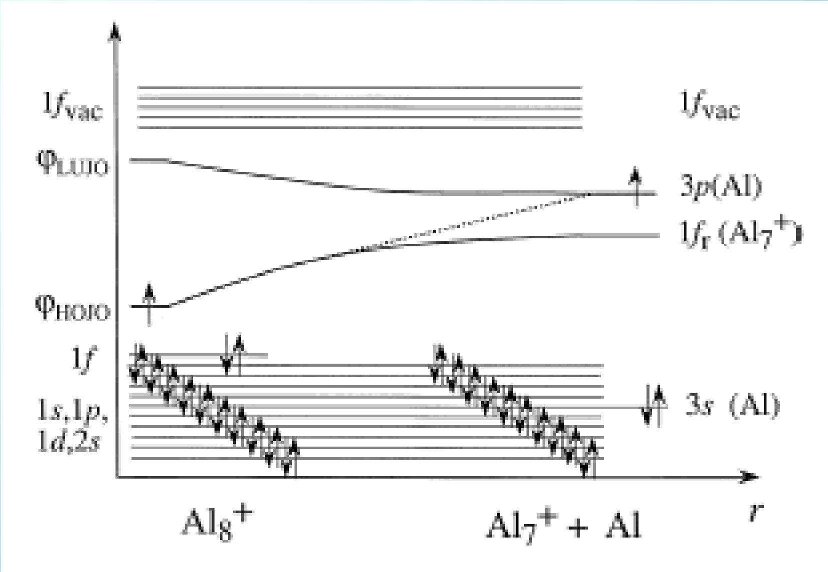

Potential energy curves along Al_8^+ - Al_7^+ + Al

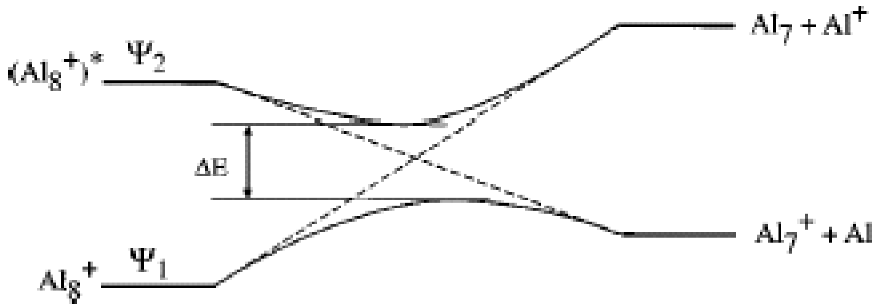

FIG. 6. Schematic potential energy curves along the reaction coordinate. The dissociation channel for the Al release is correlated to an electronic excited state, given by the wave function, Ψ_2, while the dissociation channel for the Al^+ release is correlated with the ground state of Al_8^+ , Ψ_1.

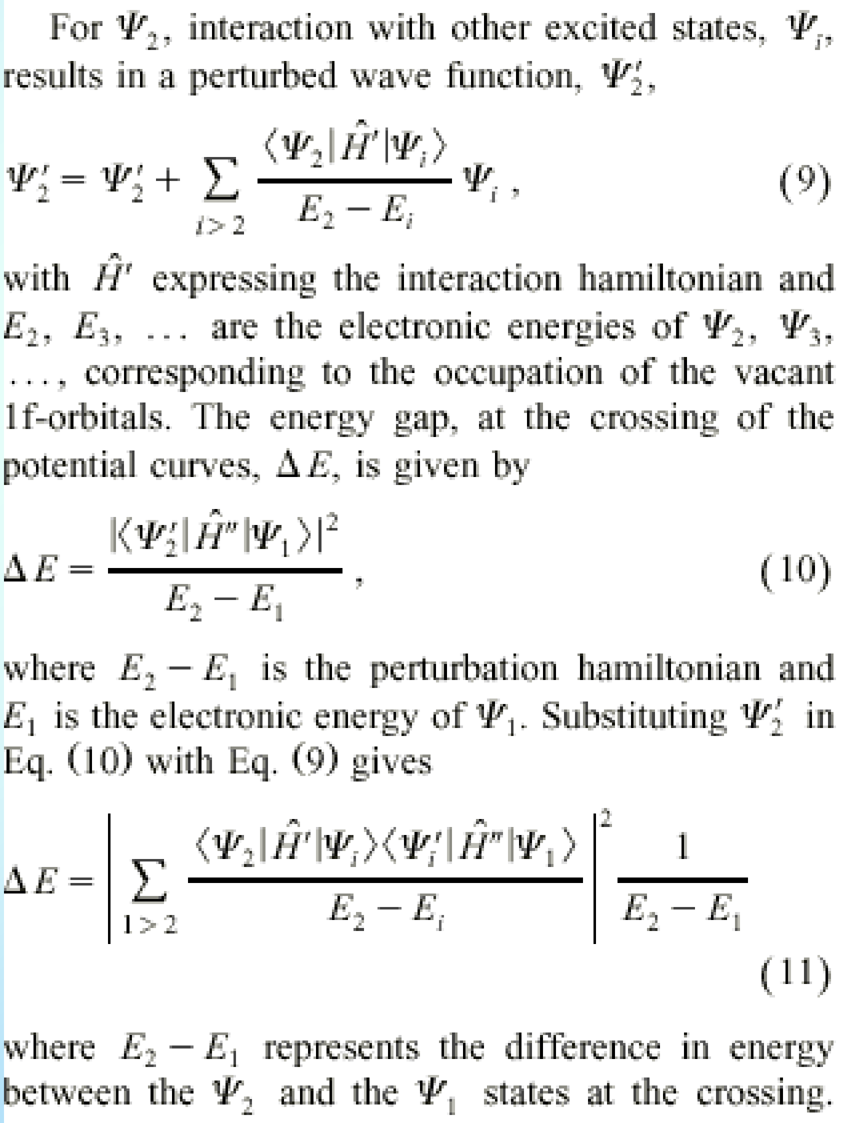

For Ψ_2, interaction with other excited states, Ψ_i, results in a perturbed wave function, Ψ_2',

$$\Psi_2' = \Psi_2' + \sum_{i>2} \frac{\langle \Psi_2 | \hat{H}' | \Psi_i \rangle}{E_2 - E_i} \Psi_i \ , \tag{9}$$

with $\hat{H}'$ expressing the interaction hamiltonian and E_2, E_3, ... are the electronic energies of Ψ_2, Ψ_3, ..., corresponding to the occupation of the vacant 1f-orbitals. The energy gap, at the crossing of the potential curves, ΔE, is given by

$$\Delta E = \frac{|\langle \Psi_2' | \hat{H}'' | \Psi_1 \rangle|^2}{E_2 - E_1} \ , \tag{10}$$

where $E_2 - E_1$ is the perturbation hamiltonian and E_1 is the electronic energy of Ψ_1. Substituting Ψ_2' in Eq. (10) with Eq. (9) gives

$$\Delta E = \left| \sum_{1>2} \frac{\langle \Psi_2 | \hat{H}' | \Psi_i \rangle \langle \Psi_i' | \hat{H}'' | \Psi_1 \rangle}{E_2 - E_i} \right|^2 \frac{1}{E_2 - E_1} \tag{11}$$

where $E_2 - E_1$ represents the difference in energy between the Ψ_2 and the Ψ_1 states at the crossing.

Dr. Oddur Ingólfsson

The University of Iceland
Professor

問.
原子･分子の衝突断面積と反応断面積との
一般的な違いについて、簡単に説明しなさい。